

*Research Articles: Neurobiology of Disease*

## **Zika Virus Infection In The Developing Mouse Produces Dramatically Different Neuropathology Dependent On Viral Strain**

<https://doi.org/10.1523/JNEUROSCI.1376-19.2019>

**Cite as:** J. Neurosci 2019; 10.1523/JNEUROSCI.1376-19.2019

Received: 20 June 2019

Revised: 27 November 2019

Accepted: 9 December 2019

---

*This Early Release article has been peer-reviewed and accepted, but has not been through the composition and copyediting processes. The final version may differ slightly in style or formatting and will contain links to any extended data.*

**Alerts:** Sign up at [www.jneurosci.org/alerts](http://www.jneurosci.org/alerts) to receive customized email alerts when the fully formatted version of this article is published.

**Title:** Zika Virus Infection In The Developing Mouse Produces Dramatically Different Neuropathology Dependent On Viral Strain

**Abbreviated Title:** Zika virus-induced neuropathology in the mouse

**Authors:** Kevin K. Noguchi, Ph.D.<sup>1\*</sup>, Brant S. Swiney<sup>1</sup>, Sasha L. Williams M.A.<sup>1</sup>, Jacob N. Huffman M.A.<sup>1</sup>, Katherine Lucas<sup>1</sup>, Sophie H. Wang<sup>1</sup>, Kayla M. Kapral<sup>1</sup>, Amber Li<sup>1</sup>, Krikor T. Dikranian, M.D., Ph.D.<sup>2</sup>

<sup>1</sup>Department of Psychiatry, Washington University in St Louis, 63110

<sup>2</sup>Department of Neuroscience, Washington University in St Louis, 63110

**Pages:**54

**Figures:** 12

**Tables:** 1

**Words:** Abstract: 145, Introduction: 647, Discussion 1355

**Conflict of interest:** The authors declare no competing financial interests.

**Acknowledgements:** Funding: Research in this paper was primarily supported by the Large Exploratory and Pilot Grants (K.K.N) funded by the Intellectual and Developmental Disabilities Research Center (IDDRC) at Washington University (IDDRC@WUSTL Research Program) in addition to NIH grant (NICHD U54-HD087011) for the IDDRC at Washington University. The authors would also like to thank Dr. Michael Diamond and his lab (particularly Jen Govero) for their support and advice in the design and implementation of these studies. Electron microscopic imaging was performed at the Washington University Center for Cellular Imaging (WUCCI) supported by Washington University School of Medicine, The Children's Discovery Institute of Washington University, St. Louis Children's Hospital (CDI-CORE-2015-505), and the Foundation for Barnes-Jewish Hospital (3770).

**\*To whom correspondence should be addressed:**

Kevin K. Noguchi, Ph.D.  
Assistant Professor of Psychiatry  
Washington University in St. Louis  
Department of Psychiatry  
4559 Scott Avenue  
St. Louis, MO 63110  
noguchik@wustl.edu  
(O) 314-362-7007

44 **ABSTRACT**

45 Zika virus (ZIKV) infection during pregnancy has been causally linked to a constellation of  
46 neurodevelopmental deformities in the fetus resulting in a disease termed Congenital Zika  
47 Syndrome (CZS). Here we detail how ZIKV infection produces extensive neuropathology in the  
48 developing mouse brain and spinal cord of both sexes. Surprisingly, neuropathology differs  
49 depending on viral strain with a French Polynesian isolate producing primarily excitotoxicity and  
50 a Brazilian isolate being almost exclusively apoptotic but occurring over a prolonged period that  
51 is more likely to produce severe hypoplasia. We also show exposure can produce a  
52 characteristic pattern of infection that mirrors neuropathology and ultimately results in gross  
53 morphological deformities strikingly similar to CZS. This research provides a valuable mouse  
54 model mirroring the clinical course of disease that can be used to test potential therapies to  
55 improve treatment and gain a better understanding of the disabilities associated with CZS.

56

57

58

59

60

61

62

63

64 **SIGNIFICANCE STATEMENT**

65 Zika virus (ZIKV) infection during pregnancy has been causally linked to a constellation of  
66 neurodevelopmental deformities in the fetus resulting in a disease termed Congenital Zika  
67 Syndrome. Despite its devastating effects, very little is known about how ZIKV infection  
68 produces fetal neuropathology. Here we detail the temporal progression of ZIKV infection in the  
69 mouse brain and spinal cord resulting in massive neurodegeneration of infected regions. We  
70 also report a ZIKV strain from a region of Brazil with high levels of microcephaly (abnormally  
71 small head circumference) produces particularly devastating neuropathology.

72

73 **INTRODUCTION**

74 First discovered in the Ugandan Zika forest in 1947, the Zika virus (ZIKV) initially produced  
 75 sporadic outbreaks throughout Africa and Asia before causing major epidemics in Micronesia  
 76 and French Polynesia where there was concern human infection was producing Guillain-Barre  
 77 syndrome (Cao-Lormeau et al., 2016; Lazear et al., 2016). In 2015, interest increased  
 78 dramatically once ZIKV infection was correlated with a dramatic increase in microcephaly  
 79 resulting in at least 1950 confirmed cases in Brazil alone. While definitions vary, microcephaly  
 80 is a medical condition in which a baby is born with an abnormally small head circumference.  
 81 The Centers for Disease Control has subsequently established a causal relationship between  
 82 ZIKV infection and microcephaly (Rasmussen et al., 2016) which was followed by their most  
 83 difficult emergency health response ever undertaken (Beck, 2016). While research initially  
 84 focused on microcephaly, clinicians now use the term Congenital Zika Syndrome (CZS) to  
 85 highlight the constellation of symptoms ZIKV infection can produce during neurodevelopment.  
 86 Symptoms of CZS include microcephaly, calcifications, epileptic seizures, arthrogryposis, and  
 87 neuromotor deficits (Saad et al., 2018). Additionally, while estimates suggest hundreds of  
 88 thousands of women were infected during their pregnancy (Adams Waldorf et al., 2018), it is  
 89 unknown if undetected fetal pathology occurred that will manifest later with age. Since CZS is a  
 90 newly discovered disease, its long-term effects are unknown but will undeniably lead to a  
 91 lifetime of severe intellectual disability for many affected. With a lifetime price of care estimated  
 92 at \$10 million per effected individual (Frieden et al., 2016), the total financial cost for these  
 93 children will likely be enormous.

94 Despite the devastating effects of this disease, we still know little about how infection leads  
 95 to neuropathology or whether virulence differs between strains. While current research  
 96 suggests ZIKV infection can destroy neural progenitor cells and reduce neurogenesis, this  
 97 would not explain why microcephaly can occur following third trimester infection (Brasil et al.,  
 98 2016) or develop postnatally after normocephalic birth (van der Linden et al., 2016b) when

almost all cerebral neurogenesis is complete (de Graaf-Peters and Hadders-Algra, 2006). Another mystery is why the ZIKV was only associated with microcephaly following the 2015 Brazilian outbreak despite its discovery in 1947. One reason may be an adaptive mutation that increased infectivity in neural progenitor cells (NPCs) resulting in more significant microcephaly (Yuan et al., 2017). This mutation occurred just prior to the 2013 French Polynesian outbreak and has remained unaltered in subsequent epidemics as the virus spread to Brazil and the rest of the Americas. However, there are differences in microcephaly rates after this time. The 2015 Brazilian outbreak resulted in infections throughout the country, yet 83.3% of all microcephalic cases were concentrated in a small northeastern region of the country (de Oliveira et al., 2017b). As a result, important epidemiological questions remain as to whether differences in neuropathology between strains may be responsible for drastically differing microcephaly rates. Others have reported infection of juveniles or adults with African strains produce more severe pathology than Asian strains (Duggal et al., 2017; Tripathi et al., 2017). Additionally, direct intracerebral infection of newborns pups with a more contemporary Venezuelan strain has been reported to produce more severe microcephaly than an ancestral Cambodian strain. However, we are unaware of studies that directly compare differences between the Brazilian strain and others that may explain the high rates of microcephaly following the 2015 Brazilian outbreak. Based on this information, we examined the neuropathology produced in the developing rodent brain following infection with clinical isolates from French Polynesia or Paraiba - the northeastern Brazilian state where microcephaly rates were highest (Jaenisch et al., 2017). Our findings reveal that exposure produces a characteristic pattern of infection resulting in extensive neuropathology that result in gross morphological changes strikingly similar to CZS. We further discovered different strains produce different types of pathology with the Brazilian strain being far more virulent and more likely to produce gross morphological changes consistent with microcephaly.

124

125 **MATERIALS AND METHODS**

126 Experimental design and statistical analysis: We examined the ability of two ZIKV strains to  
 127 induce neuropathology in wild-type C57BL/6J developing mice. All experiments included both  
 128 male and female mice, but this was not tracked for statistical analysis. Animals were first  
 129 examined for neuropathology using silver staining (detects all types of degeneration) and  
 130 activated caspase-3 (AC3; detects only apoptosis). For each strain and days post infection  
 131 (DPI) timepoint, at least two litters were examined to ensure consistent results. This information  
 132 was then used to further examine infection pattern and type of neuropathology using a variety of  
 133 methods. Histology and assessments were done blind to treatment. All procedures were  
 134 approved by the Washington University in St. Louis Institutional Animal Care and Use  
 135 Committee in accordance with the Guide for the Care and Use of Laboratory Animals (Anon,  
 136 2011). Sample sizes were based on experience using similar analysis in previous studies  
 137 (Noguchi et al., 2008; Cabrera et al., 2016) to gain enough power to detect statistically  
 138 significant differences if present. Since quantification is performed in several brain regions, it  
 139 can be argued we need to control for multiple comparisons. We therefore applied a Bonferroni  
 140 correction for multiple comparisons by dividing the  $\alpha$  level ( $\alpha = 0.05$ ) by the number of  
 141 comparisons for AC3 ( $\alpha < 0.0071$ ), silver staining ( $\alpha < 0.0071$ ), and area measurements ( $\alpha <$   
 142  $0.013$ ). Statistical tests that would become non-significant following correction are indicated in  
 143 Table 1. It should be noted this correction is very conservative and increases the chance of  
 144 false negatives (an error in which significant result becomes non-significant)(Lindquist and  
 145 Mejia, 2016). More detailed descriptions of experimental design and statistical analysis can be  
 146 found in the subsections below.

147 Zika Virus: The H/PF/2013 (French Polynesia, 2013; **FP/2013**) and Paraiba (Brazil, 2015;  
 148 **Paraiba/2015**) ZIKV strains were a kind gift from the laboratory of Michael Diamond who

149 obtained them from the Arbovirus Branch of the Centers for Disease Control and Prevention or  
 150 Steve Whitehead (NIH) respectively. Virus was propagated and maintained as described  
 151 previously (Miner et al., 2016a) by propagating in Vero cells, titrating using a focus-forming  
 152 assay, and storing in aliquots at -80 °C. Neonatal mice were intraperitoneally inoculated with  
 153  $10^3$  FFU in a volume of 25  $\mu$ L and immediately returned to dams. Mock infection was carried  
 154 out by injecting an equal volume of vehicle alone. All neonates within a litter received the same  
 155 treatment (infected or mock infected) to eliminate the possibility of cross infection between pups.

156 Silver Staining: The de Olmos cupric silver staining procedure is a sensitive method for  
 157 staining degenerating cells (DeOlmos and Ingram, 1971; Noguchi et al., 2005; Creeley et al.,  
 158 2013). For silver staining and immunohistochemistry, treated animals were sacrificed at  
 159 different DPI by deep anesthesia prior to transcardial perfusion with 4% paraformaldehyde in  
 160 TRIS buffer (pH 7.4) and, after postfixation, brains were sectioned on a vibratome (DSK  
 161 Microslicer DTK-1000N) at 75  $\mu$ M in the coronal (cerebrum) or sagittal (cerebellum) plane.  
 162 Silver staining was performed in free floating sections as described previously (DeOlmos and  
 163 Ingram, 1971; Noguchi et al., 2005) by washing sections in distilled deionized water,  
 164 preincubating in a cupric-silver solution overnight after heating to 33° C, washing in acetone,  
 165 incubating for 35 minutes in a silver diamine solution, reduction using formaldehyde/citric acid,  
 166 washing with distilled water, bleaching with 0.3%  $K_3Fe(CN)_6$ , and stabilizing using  $Na_2S_2O_3$ .

167 Immunohistochemistry: Immunolabeling with polyclonal antibodies was performed by  
 168 quenching sections in 3% hydrogen peroxide/methanol, blocking in 2% BSA/0.2% milk/0.1%  
 169 Triton X-100 mixture in PBS, and incubation in primary antibody overnight. The next day,  
 170 sections were then reacted with ABC reagents (Vectastain ABC Elite Kit) prior to chromogen  
 171 labeling with VIP (Vector VIP). All primary antibodies used were rabbit polyclonal: Activated  
 172 caspase-3 (Cell Signaling Technology Inc., Danvers, MA, USA; Cat# 9661L; 1:1000); Iba1  
 173 (Wako Chemicals, Richmond, VA, USA; Cat# 1919741; 1:15,000; RRID: AB\_839504) It should  
 174 be noted that viral infection can increase endogenous Fc receptor binding resulting in false



175 positive labeling during immunohistochemistry. We examined this possibility in a pilot study and  
 176 found ZIKV infection does indeed produce false positive labeling of microglia when mouse  
 177 monoclonal antibodies were used even in the absence of primary antibodies. Interestingly,  
 178 rabbit polyclonal antibodies raised against different epitopes labeled unique populations of cells  
 179 indicating they do not produce false positive labeling. This makes sense in that the mouse Fc  
 180 receptor would selectively bind to mouse antibodies and not those from other species. Based  
 181 on this information we avoided using mouse monoclonal antibodies in these studies.

182 Kaplan-Meier curves: Animal survival was tracked in mice (n = 137) to produce Kaplan-  
 183 Meier Curves (Goel et al., 2010; Rich et al., 2010) following P1 infection by noting the DPI when  
 184 death (or sacrifice due to suffering) or censorship (planned sacrifice to perform histology)  
 185 occurred until 30 DPI. Results were entered into Prism statistical software (version 5.0a) and  
 186 analyzed using the Gehan-Breslow-Wilcoxon Test and Log-rank (Mantel-Cox) Test for survival  
 187 analysis.

188 Semi-Quantitative Analysis: Stereological analysis was impossible following some  
 189 treatments because pathology became so intense that heavy degeneration occurred throughout  
 190 entire regions preventing discrimination of individual cells. We therefore had a rater, blind to  
 191 treatment, semi-quantitatively rate the amount of degeneration on slides stained with either  
 192 activated caspase-3 or silver staining at either 7, 13, or 30 DPI following either mock (n = 23),  
 193 **FP/2013** (n = 16), or **Paraiba/2015** (n=22) infection. For each animal, both stains were  
 194 performed in three coronal sections corresponding to +0.02 mm bregma, -1.755 mm bregma,  
 195 and -2.98 mm bregma respectively in addition to one midsagittal section (0.0 mm lateral) of the  
 196 cerebellum (Lein et al., 2007). The amount of degeneration was then semi-quantitatively  
 197 evaluated in the hippocampus, motor cortex, visual cortex, striatum, thalamus, cerebellum, and  
 198 septum based on a five point Likert scale using the following criteria: 1 = slight to no  
 199 degeneration, 2 = moderate degeneration, 3 = significant degeneration, 4 = high amounts of

200 degeneration, and 5 = intense degeneration (continuous regions of degeneration where  
201 individual cells are not discernible).

202 Quantification of brain regions and weight: Quantification of brain weight and brain regional  
203 areas were performed in animals exposed to the **FP/2013** (n=4), **Paraiba/2015** (n=7), or mock  
204 (n=11) infection and sacrificed on 30 DPI. Whole brain weights were measured following  
205 removal from the skull prior to sectioning. Brains were then vibratome cut at 75  $\mu$ M and regional  
206 area quantified on four Nissl stained sections (0.1% cresyl violet acetate in 0.3% v/v glacial  
207 acetic acid) corresponding to the same regions used for semi-quantitative analysis. Areas were  
208 calculated by tracing regions using Stereo Investigator Software (Version 2019, MBF  
209 Bioscience, Williston, Vermont) connected to a QImaging 200R camera on a Nikon Labophot-2  
210 microscope using a 4X objective. The dorsal cortex, hippocampus, and lateral ventricles were  
211 traced on coronal sections and the cerebellum from the sagittal section. The dorsal cortex  
212 included all cortex dorsal to the piriform/entorhinal cortex and was chosen due to the isolated  
213 degeneration in this region. Regions occurring in multiple sections had areas summed prior to  
214 statistical analysis. All quantification was analyzed using one- or two-way ANOVAs and  
215 Bonferroni posthocs using Prism statistical software (version 5.0a).

216 In Situ Hybridization: Animals were perfused with 4% paraformaldehyde in TRIS buffer (pH  
217 7.4) and dissected to remove brain and spinal cord. Tissue was post-fixed overnight,  
218 dehydrated with graded alcohols, stored in 70% ethanol, embedded in paraffin, cut at 5  $\mu$ M,  
219 dried overnight, and deparaffinized. ZIKV RNA labeling was performed using a Advanced Cell  
220 Diagnostics HybEZ II Oven with ZIKV probe (Cat#: 468361) and visualized with a RNAScope  
221 2.5 HD Red Assay (Cat#: 322360) and hematoxylin counterstaining. For ISH/immunolabeling  
222 combined technique, ISH for ZIKV RNA was performed first followed by immunolabeling with  
223 antibodies for neurons (NeuN; 1:100, Millipore; Cat#:ABN78; RRID:AB\_10807945), microglia  
224 (Iba1; 1:15,000, Wako Chemicals, Cat#:1919741; 1:15,000; RRID: AB\_839504), or astrocytes  
225 (GFAP; 1:400, Sigma-Aldrich, Cat#: G9269; RRID:AB\_477035) prior to coverslipping. The ISH

226 red assay used for bright field images also fluoresces in the red channel without bleeding into  
227 the other channels.

228 Plastic Embedding and Electron Microscopy: Animals were first transcardially perfused  
229 with 1.5% glutaraldehyde/1% paraformaldehyde following deep anesthesia. Brains were then  
230 removed, cut into 1 mm slabs in the coronal plane, osmicated with 1% osmium tetroxide  
231 overnight, placed in graded alcohol to dehydrate, cleared in toluene, and finally plastic  
232 embedded in araldite. For semithin sections, tissue was then cut using a Leica Ultracut UCT  
233 ultramicrotome at 1  $\mu$ M and stained with Azure II/Methylene blue. For electron microscopy,  
234 sections were suspended over a formvar coated slot grid prior to staining with uranyl  
235 acetate/lead citrate and visualized using a JOEL JEM1400 transmission electron microscope.

236 Alizarin Staining: Alizarin is a standard chemical dye for the detection of calcifications in  
237 the brain. A 2% Alizarin Red S (Sigma Aldrich, St Louis, USA) solution was prepared by mixing  
238 in 0.1M borate buffer, filtering a 0.45  $\mu$ M, and adjusting pH to 6.7. Slide mounted sections were  
239 then immersed in alizarin solution for 1 hour, rinsed by dipping in tap water for 20 dips, and  
240 cleared in 70% ethanol for 20 dips. Tissue was then dehydrated for 2 minutes in 95%, 95%,  
241 100%, and 100% ethanol baths followed by immersion in three changes of citri-solve for 5  
242 minutes before coverslipping.

243 Imaging: Bright field and fluorescent photocomposites were taken on Leica DM400B  
244 microscope with a Leica DFC310FX camera using Surveyor software V7.0.0.6 MT (Objective  
245 Imaging, Cambridge, UK) to photomerge images. For fluorescent images, each channel was  
246 imaged individually and merged in Adobe Photoshop (V 12.0) after adjustment of channel  
247 levels.

248 Viral Sequences: Viral sequences for **FP/2013** (KJ776791.2) and **Paraiba/2015**  
249 (KX280026.1) were obtained from the National Institutes of Health's Genbank  
250 (<https://www.ncbi.nlm.nih.gov/genbank/>) for comparison (Baronti et al., 2014; Tsetsarkin et al.,  
251 2016). Missense and untranslated region mutations are discussed however, while there were

252 numerous synonymous mutations, they were not mentioned since they are more likely to be  
 253 silent.

## 254 255 **RESULTS**

### 256 **Infection and Behavior**

257 To examine the time course of neuropathology following infection, neonatal wild-type C57BL/6  
 258 mice of both sexes were inoculated with  $10^3$  focus forming units (FFU) of clinical isolates from  
 259 the 2013 French Polynesian (H/PF/2013; **FP/2015**) or 2015 Paraiba Brazilian outbreaks  
 260 (**Paraiba/2015**) as described previously (Miner et al., 2016a, 2016b). Injections were  
 261 administered between postnatal days 1-4 as a single intraperitoneal injection (van den Pol et al.,  
 262 2017). It is important to note that because the mouse is born neurodevelopmentally immature  
 263 compared to the human, a newborn pup brain is the equivalent of a human fetus in the early  
 264 second trimester of gestation (Clancy et al., 2007; Workman et al., 2013). Mock infected control  
 265 mice were intraperitoneally injected with only vehicle at an equal volume. Behaviorally, some  
 266 animals displayed motor deficits which, if present, resulted in an unsteady gait or falling during  
 267 ambulation and an inability or difficulty to perform a righting reflex once placed in a supine  
 268 position around 10 DPI. Ataxia progressively worsened afterwards and was followed by flaccid  
 269 paralysis of hindlimbs as animals became moribund by around P14.

### 270 271 **FP/2013 and Paraiba/2015 produce different Kaplan-Meier curves**

272 We first generated Kaplan-Meier curves for the **FP/2013** and **Paraiba/2015** strains  
 273 following P1 infection until 30 DPI (**Figure 1A**). While both strains were almost equally lethal,  
 274 most deaths occurred between 10-17 DPI for **FP/2013** but this period was more evenly  
 275 distributed and expanded between 8-24 DPI for **Paraiba/2015**. Survival curves are typically  
 276 analyzed by the Gehan-Breslow-Wilcoxon Test or the Log-rank Mantel-Cox Test. The former is

277 sensitive to deaths early in the survival curve while the latter is more powerful if the chance of  
 278 death is the same at all time points. Interestingly, the Gehan-Breslow-Wilcoxon Test was  
 279 statistically significant ( $\chi^2 = 10.33$ ,  $p < 0.001$ ) but the Log-rank Mantel-Cox Test was not ( $\chi^2 =$   
 280  $2.366$ ,  $p > 0.05$ ). This suggests lethality following **FP/2013** exposure is heightened during an  
 281 early acute period compared to **Paraiba/2015** that is less intense and occurs over a more  
 282 prolonged period.

283

#### 284 **French Polynesian Strain**

285 We first examined how neuropathology evolves over time by infecting mice with **FP/2013** and  
 286 sacrificing for histology at varying DPI. Neuropathology and infection were assessed using  
 287 silver staining (detects all types of cellular degeneration), activated caspase-3 (AC3)  
 288 immunolabeling (detects only apoptosis), and *in situ* hybridization (ISH) for ZIKV RNA (to  
 289 measure the pattern of infection). Neuropathology was then quantified using a semi-quantitative  
 290 degeneration scale on 7, 13, and 30 DPI in sections labeled with AC3 (**Figures 1B-H**) and silver  
 291 staining (**Figures 1I-O**). Finally, the long-term effects of infection on hypoplasia was quantified  
 292 by determining brain weight (**Figures 1P**) and outlining specific regions to determine or area at  
 293 30 DPI (**Figure 1Q-T**). Data was then analyzed using one- or two- way ANOVAs followed by  
 294 Bonferroni post-hoc analysis (**Figure 1** and **Table 1**).

295

#### 296 **FP/2013 Infection: Early Stage - 7 to 13 DPI**

297 Neuropathology began as early as 7 DPI but was more consistently seen by 13 DPI. In general,  
 298 while AC3 and silver staining tended to overlap, only silver staining could detect degeneration at  
 299 7 DPI suggesting non-apoptotic degeneration was occurring during this early stage (**Figures**  
 300 **1B-O**).

301 Dorsal Cortex: Degeneration in the dorsal cortex included the motor, somatosensory,  
 302 retrosplenial, and visual cortices. By 10-13 DPI, advanced degeneration involved all layers with  
 303 heavier bilaminar degeneration in layer IV and the ventral portion of layer V that seemed  
 304 particularly intense in the somatosensory cortex (**Figures 1B-C,I-J and 2A-D,G-J**). The ventral  
 305 cortex was relatively spared but degeneration could be seen in some animals at more advanced  
 306 stages. ISH for ZIKV RNA revealed cortical infection mirroring argyrophilia (silver positive  
 307 degeneration) with a similar bilaminar appearance (compare **Figures 2A,G** with **2E,K**) and often  
 308 showed cellular profiles of soma that resembled pyramidal cells (**Figure 2F**). Interestingly,  
 309 clinical research has found a similar bilaminar pattern of infection in the dorsal cortex of ZIKV  
 310 infected fetuses (Bhatnagar et al., 2017) suggesting a similar pattern of infection between  
 311 species. No similar neuropathology was seen in mock infected controls (**Figures 2C-D and 2I-**  
 312 **J**).

313 Visual Regions: Consistent with our previous research suggesting the ZIKV can gain entry  
 314 through visual pathways (Miner et al., 2016b), one of the first regions to show degeneration is  
 315 the optic tract and lateral geniculate nucleus (LGN; visual relay center in the thalamus) around 7  
 316 DPI (**Figures 2G-J, Figures 3A-B**). This complements previous research showing neonatal  
 317 ZIKV inoculation produces infection in the retina first that spreads to the LGN (van den Pol et  
 318 al., 2017). This is also consistent with the high incidence of retinal/optic nerve degeneration  
 319 (Miner et al., 2016b) and visual impairment in CZS children (Ventura et al., 2018) suggesting  
 320 viral infection occurs similarly between species. As infection progressed, other visual areas  
 321 degenerate including the superior colliculus and visual cortex (**Figures 1C,J and 2G-J**).  
 322 Infection mirrored silver staining with early punctate ISH labeling in the optic tract (compare  
 323 **Figures 3A and 3C**) followed by the LGN and visual cortex (**Figures 2K-L**).

324 Hippocampal Formation: Injury in the hippocampal formation was usually absent at 7 DPI  
 325 but became severe at later stages suggesting this was not the primary site of infection (**Figure**  
 326 **1D,K**). The most consistent degeneration was in the dentate gyrus where argyrophilia was

327 seen in granule cells and the molecular layer neuropil connecting granule cell dendrites to  
 328 perforant path axon terminals (**Figures 2G-J, Figures 3D-E**). Degeneration also occurred less  
 329 frequently in CA3 and CA1 pyramidal cells (**Figures 2G-J**). Interestingly, these structures form  
 330 a trisynaptic circuit with granule cells sending afferents through the mossy fibers to CA3 and  
 331 CA3 connecting to CA1 through Scheaffer collaterals (**Figures 3D-E**). This may suggest the  
 332 virus spreads transynaptically through connected regions. Closer examination revealed a large  
 333 number of degenerating microglia in the dentate polymorph layer, stratum oriens, and stratum  
 334 radiatum (**Figures 2G-J and Figures 3D-E**). Hippocampal infection also closely mirrored  
 335 microglial and neuronal death (compare **Figures 2G-H with 2K-L and Figures 3D with 3F**).  
 336 Clearly ISH labeled granule cell and pyramidal cell neurons could be seen in the dentate gyrus  
 337 and CA1/CA3 respectively (**Figures 2K-L**). While infection also occurred in regions with  
 338 microglial degeneration in the polymorph layer, stratum oriens, and stratum radiatum, it was  
 339 difficult to determine cell type.

340 Cerebellum: The cerebellum was one of the most heavily affected regions (**Figures 1E,L**).  
 341 It actually contains more neurons than the cerebrum with the vast majority being granule cell  
 342 neurons that send axons to the superficial molecular layer where they bifurcate in opposite  
 343 directions before synapsing with dendrites from multiple Purkinje cells. Extensive argyrophilia of  
 344 both granule and Purkinje cells were seen along with degenerating neuropil of their synaptic  
 345 connections in the molecular layer (**Figures 2M-P**). The cerebellum also exhibited high ZIKV  
 346 RNA in the molecular, Purkinje, and granule cell layers similar to argyrophilia (compare **Figures**  
 347 **2M-N with 2Q-R**). ISH labeled Purkinje cells were identifiable due to their characteristic large  
 348 size and position but it was difficult to definitively identify other infected cell types (**Figure 2R**).

349 Spinal Cord: Since layer V somatosensory cortex is injured and sends numerous afferents  
 350 to the corticospinal tract (even more than the motor cortex in the mouse (Sengul and Watson,  
 351 2015)) we next examined the spinal cord. Degeneration occurred in the grey matter but was  
 352 more extensive in the funiculus (white matter). The most conspicuous degeneration was in the



353 corticospinal tract which is consistent with fetal CZS autopsies showing this pathway is often  
 354 shrunken or missing (**Figures 2S-T**) (Chimelli and Avvad-Portari, 2018). Activated caspase-3  
 355 immunolabeling revealed corticospinal toxicity was primarily apoptotic and encompassed large  
 356 portions of this tract (**Figure 2U**). Infection was also heavy in the funiculus which contains  
 357 numerous ascending and descending pathways such as the corticospinal, vestibulospinal,  
 358 reticulospinal, and spinothalamic tracts (**Figure 2V**). The spinal grey also exhibited infection to  
 359 a lesser degree. The spinal cord was one of the earliest regions to show infection suggesting a  
 360 secondary route of neuroinvasion. This could be seen as punctate labeling in the cytoplasm  
 361 surrounding the nucleus of some cells in the spinal lateral horn around 7 DPI (**Figure 3G**).  
 362 Interestingly, the herpes virus also gains entry to the brain through the visual and spinal  
 363 (corticospinal) pathways suggesting a similar route of neuroinvasion (Lewis et al., 1989;  
 364 Kidokoro et al., 2017).

365 Other Regions: Neuropathology could also be seen in other regions including the  
 366 thalamus, caudate/putamen, septum, and subiculum (**Figures 1F-H, 1M-O, 2A-D and 2G-J**)  
 367 which mirrored infection (**Figures 2E-F and K-L**).

368

### 369 **Early neurodegeneration is excitotoxic**

370 Early neuropathology includes limited apoptosis: Once we established the pattern of  
 371 degeneration/infection, we next examined differences in neuropathology. We first applied both  
 372 silver staining and AC3 immunolabeling on sections from the same animal and region. AC3  
 373 was highly correlated with regional silver staining but exhibited far fewer cellular profiles in most  
 374 regions (**Figure 4**). Silver staining also marked some cell types not seen with AC3 staining  
 375 such as microglia and Purkinje neurons. Both stains labeled the corticospinal tract that was  
 376 more distinct with AC3 immunolabeling and often involved large portions of this pathway as it  
 377 projected from the cortex ventrally as the internal capsule and continued into the spinal cord



378 (Figures 4C-D and 4G-J). From this comparison, we conclude ZIKV infection produces  
379 significant apoptosis but there is also extensive non-apoptotic death occurring.

380 Plastic embedding reveals vacuolization and apoptosis: To examine this non-apoptotic  
381 death further, we plastic embedded tissue (which preserves the fine micro- and ultra- structural  
382 morphology in greater detail) and stained with the nuclear stain Azure II/Methylene blue. The  
383 hippocampal formation exhibited heavy neuropathology including large regions of neuronal  
384 vacuolization (fluid filled cavities within the cytoplasm) and abnormal nuclear chromatin  
385 condensation in the granule cells of the dentate gyrus (Figure 5A). Similar vacuolization could  
386 be seen in the pyramidal cells of CA3/CA1 intermixed with lower amounts of apoptosis along  
387 with dendritic swelling in the stratum oriens dorsal to the CA region (Figure 5B). Beyond the  
388 hippocampus, the cortex also exhibited large regions of heavy vacuolization interspersed with  
389 pyknotic apoptotic cells (Figure 5C). None of this pathology could be seen in mock infected  
390 controls in the same regions (Figures 5D, E, F respectively).

391 Neuronal excitotoxicity and microglial degeneration: Since we were approaching  
392 magnification limits of the microscope, we next examined plastic embedded tissue using  
393 electron microscopy. In the cortex, neurons in an early phase of degeneration exhibited  
394 cytoplasmic condensation, swelling of granulated endoplasmic reticulum, and nuclear  
395 margination where clumps of aggregated chromatin localize to the inner edge of the nuclear  
396 envelope (called a "clock-face" profile; compare Figures 5G with 5H). This is often  
397 accompanied by condensation of cytoplasm leading to compaction of organelles, vacuolization  
398 as the endoplasmic reticulum swells, and further vacuolization of the nuclear envelope (Figures  
399 5H-I). Similar pathologic changes could be seen in the dentate gyrus granule cells (Figure 5J)  
400 and CA1 hippocampal pyramidal cells (Figure 5K) consistent with Azure II/Methylene blue  
401 staining. Importantly, the dendritic swelling, nuclear margination, and vacuolization we see are  
402 all classical hallmarks of excitotoxicity - the pathological process by which neurons are  
403 damaged or killed by glutamatergic overstimulation (Ishimaru et al., 1999). Tissue ultrastructure

also revealed other signs of an injured brain including parenchymal hemorrhage (**Figure 5L**) where leaking red blood cells can be seen in extravascular space similar to clinical reports (Brasil et al., 2016). While lymphocytes are rarely seen in the healthy brain, numerous could be seen in infected brains (**Figure 5M**) suggesting an adaptive immune response following viral infection. Finally, we also found degenerating microglia (**Figure 5N**) suggesting infection is additionally toxic to this cell type consistent with our microscopic examination.

*Infection produces microglial activation and fragmentation as microglia degenerate:* Since silver staining and ultrastructural examination revealed microglial pathology, we next immunolabeled for the microglial marker Iba1 at different DPI. Uninfected controls displayed evenly distributed ramified (resting) microglia with thin extended processes (**Figures 6A-B**) that became activated (thickened retracted processes connected to distended soma) following infection by 7 DPI (**Figures 6C-D**). By 10 DPI, regions with high amounts of degeneration either displayed microglia fragmenting into cellular debris or were more sparsely populated (**Figures 6E-F**) suggesting microglial pathology.

#### **FP/2013 Infection: Late Stage: - 13 to 30 DPI**

*Neuropathology either clears or transitions to apoptosis around 13 DPI:* After around 13DPI, infection and degeneration will decrease into smaller focal regions before being eliminated completely for most animals. However, a small number of animals will have neuropathology increase dramatically and shift to heavy apoptosis around 13 DPI. When cortical degeneration transitions to apoptosis, it expands to all layers but is still highly restricted dorsally (**Figures 7A-D**). Hippocampal apoptosis was primarily restricted to large numbers of neurons in the dentate gyrus, CA1, and CA3 although microglial degeneration can also be seen with silver staining (**Figures 7E-H**). Apoptosis in the cerebellum gradually became more dense until focal regions of degeneration were seen in large sections of the granule cell layer (**Figures 7I-L**). Compared to earlier stages of pathology, degeneration transformed from more granular degeneration of

individual cells to dense sections of apoptotic tissue dying en masse. This may suggest the virus can more easily spread in these regions to adjacent cells (regardless of cell type) rather than exclusively spreading transsynaptically. By 30 DPI, animals exhibit no evidence of continuing degeneration (**Figures 1B-O**). Some animals appear to show gross morphological changes including cortical thinning (**Figures 7M-O**), hippocampal/cerebellar hypoplasia (**Figures 7N-P**), and ventriculomegaly (**Figures 7M-O**). However, brain weight and quantification of regional areas was not significantly decreased suggesting this transition to more severe pathology is uncommon (**Figures 1P-T**).

#### **Paraiba/2015 strain primarily produces apoptosis and is much more virulent**

Previous research suggests an adaptive mutation first seen in the 2013 French Polynesian outbreak increased infection of NPCs and the ability to produce microcephaly (Yuan et al., 2017). However, the subsequent Brazilian outbreak resulted in drastically different microcephaly rates with 83.3% restricted to a small northeastern region of Brazil despite ZIKV infections throughout the country. This may suggest subsequent ZIKV strains evolved to become even more neurotoxic during this outbreak. We therefore examined whether a ZIKV strain isolated from a region with high rates of microcephaly (**Paraiba/2015** isolated from northeastern Brazil) produces neuropathology similar to the **FP/2013**.

*Paraiba/2015 produces apoptosis and is more likely to produce microencephaly:* Animals were infected at  $10^3$  FFU with the **Paraiba/2015** and sacrificed at different DPI. Quantification revealed no increase in degeneration at 7 DPI that increased dramatically by 13 DPI suggesting a more gradual progression to neurotoxicity compared to **FP/2013** (**Figure 1B-O**). Degeneration began around 10 DPI with apoptosis being much more prevalent but occurring in the same set of regions (**Figures 8A-D**). Apoptosis peaks by 10-13 DPI with AC3 labeling becoming extremely dense in many regions and most brains exhibiting gross morphological

changes (**Figures 1B-O, 8E-H**). Protracted degeneration frequently led to hippocampal hypoplasia resulting in its dorsal retraction (**Figures 8F-G**) along with the beginning of cortical thinning (**Figures 8E-G**). The cerebellum also revealed greater levels of granule cell apoptosis along with hypoplasia (**Figure 8H**). By 30 DPI, increases in degeneration were frequently seen but occurred in more limited patches in the cortex, hippocampus, and cerebellum (**Figures 1B-O, Figures 8I-P**). Unlike **FP/2013**, quantification at 30 DPI revealed significant reductions in brain weight (22%) along with reduced area in the dorsal cortex (10%), hippocampus (37%), and cerebellum (57%) (**Figures 1P-S**). The cerebellar apoptosis was primarily isolated to the granule layer of certain lobes that were selectively atrophied and resulted in hypoplasia so severe it was often noticeable upon brain removal (**Figure 8L**). While lateral ventricular size was over twice the size of controls, this did not reach significance due to high variance (**Figures 1T**). ISH labeling, like apoptosis, was more intense than **FP/2013** infection but generally involved the same regions and mirrored argyrophilia (**Figure 9**). More specifically, the sparser labeling with **FP/2013** exhibited more granular infection of individual cells whereas **Paraiba/2015** exposure could produce patches of dense ISH labeling that affected all cells within it. To investigate this further, we performed immunohistochemistry for different cell type markers on tissue labeled with ISH for ZIKV RNA at 10 DPI. In areas with high infection, there were a large number of neurons (NeuN) but more limited labeling of microglia (Iba1) and astrocytes (GFAP) (**Figure 10**). This suggest neurons are the primary cell type infected.

*Plastic embedding, electron microscopy, alizarin staining, and immunolabeling:*

We next examined this pathology further by performing plastic embedding and Azure II/Methylene blue staining. Consistent with AC3 labeling, infection with **Paraiba/2015** produced massive amounts of apoptosis with the cortex, dentate gyrus, and CA1 showing shrunken soma with nuclear chromatin condensation (**Figures 11A-C**). Closer examination with electron microscopy confirmed a large number of neurons displaying the classic signs of apoptosis

(Ishimaru et al., 1999). This included reductions in soma volume along with nuclear chromatin condensation into spherical electron-dense nuclear masses (**Figure 11D**) consistent with Azure II/Methylene blue staining. At later stages, the nuclear envelope lost integrity allowing the nucleoplasmic contents to spill into the cytoplasm as the cell was broken down further (**Figure 11E**). Other ultrastructural signs of pathology/infection could be seen including parenchymal hemorrhage (**Figure 11E**), microglial phagocytosis (**Figure 11E**), axonal pathology (**Figure 11F**), and neutrophil diapedesis indicating an adaptive immune response (**Figure 11G**). Interestingly, in the CA3 region, they seemed to be more argyrophilic cells than AC3 positive cells suggesting non-apoptotic death was occurring (**Figures 12A-B**). Subsequent plastic embedding revealed cell pathology typical of both apoptosis and excitotoxicity (**Figure 12C**). Therefore, while apoptosis dominates, limited excitotoxicity is additionally present. We next examined pathology using two other methods. Since cerebellar lobes with high apoptosis developed crystal precipitate, we also performed alizarin staining and confirmed the presence of calcification (**Figure 12D**). We also performed Iba1 staining which showed a reduced density of microglia or large patches devoid of these immune cells altogether (**Figures 12E-F**). This may indicate that continued microglial degeneration can produce immunocompromised regions where virus can flourish.

## DISCUSSION

Here we provide a detailed description of the neuropathology produced by two ZIKV strains in the developing mouse brain. This revealed that **FP/2013** and **Paraiba/2015** induce pathology in a similar set of structures while producing very different neuropathology. **FP/2013**-induced neuropathology occurs in two stages with early degeneration occurring through excitotoxicity followed by intense apoptosis in a smaller set of animals that resolves by 30 DPI. Alternatively, **Paraiba/2015** progresses more slowly resulting in extensive apoptotic degeneration that reaches significance at 13 DPI and continues until at least 30 DPI. This prolonged, unrelenting

508 degeneration is consistent with the extended lethality seen in our Kaplan-Meier curves and is  
509 the likely mechanism through which **Paraiba/2015** can produce severe  
510 microencephaly/hypoplasia. Excitotoxicity can be seen following numerous types of insults  
511 including seizures, hypoxia/ischemia, traumatic brain injury, or other diseases that produce  
512 deficient cellular energy reserves. These conditions ultimately disrupt ionic gradients leading to  
513 the release of the excitatory neurotransmitter glutamate which produces excessive stimulation  
514 and the postsynaptic influx of calcium ions that activate several enzymes such as proteases,  
515 endonucleases, and phospholipases that damage the cell (McDonald and Johnston, 1990). The  
516 vacuolization we see occurs when the neuron attempts to protect itself from excessive free  
517 intracellular calcium by sequestering it in the endoplasmic reticulum or other organelles  
518 (Noguchi, 2001). This, along with dendritic swelling and chromatin margination, are classical  
519 signs of excitotoxicity which can produce degeneration distinct from apoptosis (Ishimaru et al.,  
520 1999). This suggests that as infected neurons become compromised, they release glutamate  
521 following dysregulation of neurotransmitter reserves. This is consistent with important research  
522 from two independent labs that found ZIKV infection in neuronal cell cultures results in  
523 glutamate release and excitotoxicity (Costa et al., 2017; Olmo et al., 2017; Gaburro et al., 2018).  
524 Since seizures primarily produce injury through excitotoxicity, it is also consistent with the high  
525 incidence of epilepsy in CZS (van der Linden et al., 2018). There are several potential reasons  
526 why ZIKV infection produces apoptosis. One possibility is that apoptosis is an innate immune  
527 response whereby cells commit suicide rather than host viral infection and replication. Viruses  
528 can also release proteins that inhibit apoptosis which might explain why this type of  
529 degeneration is delayed following **FP/2013** infection (Everett and McFadden, 1999). A second  
530 possibility is that neurons become so compromised, apoptosis is initiated to efficiently remove  
531 the cell using programmed cell death. Finally, apoptosis may also be initiated through  
532 transneuronal degeneration - the secondary degeneration in an uninjured neuron due to its  
533 disconnection from others (Fornito et al., 2015). Transneuronal degeneration is much more

likely to arise in the developing brain and occurs because some neurons (such as those projecting through the corticospinal tract) die off following the loss of synaptic connectivity (Torvik, 1956; Trumpy, 1971).

We also describe a characteristic pattern of infection/neuropathology that models the clinical course of CZS. This includes frequently reported CZS abnormalities such as microencephaly, calcifications, parenchymal hemorrhage, and axonal pathology. The specific pattern of effected regions are also consistent with CZS including: [1] Degeneration in the retina, optic nerve (Miner et al., 2016b) and other visual areas consistent with clinical reports of pathology in these same structures and visual impairment in 84.6% of CZS children (de Paula Freitas et al., 2016; Ventura et al., 2016, 2018). [2] Infection and pathology in the spinal cord which is consistent with spinal cord atrophy reported in 83.3% of children with CZS (Aragao et al., 2017). More specifically, we found the corticospinal tract was especially affected which is often atrophied or missing in CZS and may explain why ZIKV infection can produce arthrogryposis - a condition where weakness/paralysis of muscles *in utero* prevents movements that relieve joint pressure leading to joint deformities due to a fixed fetal position (van der Linden et al., 2016a; Aragao et al., 2017; Carod-Artal, 2018; Chimelli and Avvad-Portari, 2018). [3] Severe cerebellar hypoplasia which occurs in 52% of CZS patients (Melo et al., 2016; Meneses et al., 2017). [4] A bilaminar pattern of infection in the cortex consistent with CZS autopsies (Bhatnagar et al., 2017).

This description of ZIKV-induced neuropathology is important for several reasons. Firstly, since CZS was first recognized in 2015, current sufferers are still children and it is unknown what behavioral deficits will manifest with age. As a result, knowing what regions are vulnerable may provide important insight into possible long-term consequences of this disorder. Secondly, our research suggests it is clinically important to know the viral strain of infection since this may predict the virulence and help answer some epidemiological mysteries surrounding the ZIKV epidemic. The extensive hypoplasia produced by **Paraiba/2015** is consistent with the high rates



of microcephaly in the Brazilian region it was isolated from. Interestingly, others have infected neonatal mice (at  $10^6$  plaque forming units) with a ZIKV isolate from a region close to Paraiba and shown reduced dorsal brain area, prolonged infection, and long-term behavioral deficits (Nem de Oliveira Souza et al., 2018). This adds further evidence that strains isolated from Northeastern Brazil around 2015 may be particularly likely to produce microencephaly. Why **Paraiba/2015** produces prolonged infection and increased virulence is currently unknown but examination of its sequence reveals two missense (base pair positions 3534 and 8007) and one 3'UTR (base pair position 10392) mutations compared to the **FP/2013** strain. Since **Paraiba/2015**-induced neuropathology is prolonged, the flaviviral 3'UTR mutation may be particularly important since this region plays an important role in viral replication and evasion of the host immune response (Ng et al., 2017). Some theories additionally suggest evolution favors a biphasic pathogenic virulence that is initially high but decreases over time as the number of susceptible hosts decreases (Berngruber et al., 2013). This may explain why a second wave of infection in Brazil did not produce dramatic increases in microcephaly (de Oliveira et al., 2017a) and will be the focus of future research. Finally, our mouse model allows us to more fully characterize how the ZIKV induces neuropathology which can be used to more accurately assess potential therapies. For instance, our research shows microencephaly only occurs after prolonged and extensive degeneration. Therefore, animal models that only use this criterion may miss more subtle damage which can have clinical relevance. Consistent with this idea, the Centers for Disease Control originally reported 6% of pregnancies with evidence of infection resulted in ZIKV-associated birth defects (Honein et al., 2017), however, a follow-up study of children above 1 year of age found 14% had a birth defect and/or neurodevelopmental abnormalities possibly associated with CZS (Rice et al., 2018). This percentage may go up as children age since it is difficult to behaviorally test neurodevelopmental deficits in children this young (Davidson et al., 2016).



585        There are also at least two major limitations to this model. Firstly, neonatal infection  
586 occurred during a rodent period equivalent to the human second/third trimester when infection  
587 can still produce CZS but most cerebral neurogenesis is complete (de Graaf-Peters and  
588 Hadders-Algra, 2006; Brasil et al., 2016; van der Linden et al., 2016b). Therefore, the limited  
589 population of cerebral NPCs during this time prevents us from examining their role in disease  
590 progression. Our findings may therefore only provide insight into exposures occurring after the  
591 first trimester or first trimester infections that persist into later gestational periods. Interestingly,  
592 we found no pathology in the large population of postnatal cerebellar NPCs suggesting they  
593 play no significant role in its subsequent hypoplasia. A second limitation of our model is that our  
594 infection during the postnatal period prevents us from modeling vertical transmission that may  
595 lead to different effects on neuropathology. For instance, this may lead to different routes of  
596 neuroinvasion or allow fetal infection with ZIKV strains that may not ordinarily cross the  
597 placenta. Regardless, it is clear the prolonged degeneration we found results in severe  
598 microencephaly that closely models CZS.

599        In summary, CZS is a devastating disease that produces a unique constellation of severe  
600 neurodevelopmental disabilities effecting thousands of children. Unfortunately, due to its recent  
601 discovery, many basic questions regarding this disease and its ultimate consequences still  
602 remain unanswered. Using the developing mouse animal model, we detail for the first time how  
603 the ZIKV can produce a characteristic pattern of infection that mirrors neuropathology resulting  
604 in gross morphological abnormalities striking similar to CZS. This toxicity is more complicated  
605 than originally thought with the type and degree of neuropathology dependent on viral strain. It  
606 is hoped this information can be used to provide insight into mechanisms of strain-dependent  
607 neurotoxicity, a better understanding of the disabilities associated with CZS, and an animal  
608 model to test potential treatment regimens that more accurately models disease progression.

609

610 **REFERENCES**

- 611 Adams Waldorf KM, Olson EM, Nelson BR, Little M-TE, Rajagopal L (2018) The Aftermath of  
 612 Zika: Need for Long-Term Monitoring of Exposed Children. *Trends Microbiol* 26:729–732.
- 613 Anon (2011) Guide for the Care and Use of Laboratory Animals. Washington, D.C., D.C.:  
 614 National Academies Press.
- 615 Aragao MFV V, Brainer-Lima AM, Holanda AC, van der Linden V, Vasco Aragão L, Silva Júnior  
 616 MLM, Sarteschi C, Petribu NCL, Valença MM (2017) Spectrum of Spinal Cord, Spinal  
 617 Root, and Brain MRI Abnormalities in Congenital Zika Syndrome with and without  
 618 Arthrogryposis. *AJNR Am J Neuroradiol* 38:1045–1053.
- 619 Baronti C, Piorkowski G, Charrel RN, Boubis L, Leparç-Goffart I, de Lamballerie X (2014)  
 620 Complete coding sequence of zika virus from a French polynesia outbreak in 2013.  
 621 *Genome Announc* 2.
- 622 Beck J (2016) Zika Is the ‘Most Difficult’ Emergency Health Response Ever, CDC Official Says -  
 623 *The Atlantic*. Atl.
- 624 Berngruber TW, Froissart R, Choisy M, Gandon S (2013) Evolution of virulence in emerging  
 625 epidemics. *PLoS Pathog* 9:e1003209.
- 626 Bhatnagar J et al. (2017) Zika Virus RNA Replication and Persistence in Brain and Placental  
 627 Tissue. *Emerg Infect Dis* 23:405–414.
- 628 Brasil P et al. (2016) Zika Virus Infection in Pregnant Women in Rio de Janeiro. *N Engl J Med*  
 629 375:2321–2334.
- 630 Cabrera OH, O'Connor SD, Swiney BS, Salinas-Contreras P, Manzella FM, Taylor GT, Noguchi  
 631 KK (2016) Caffeine combined with sedative/anesthetic drugs triggers widespread  
 632 neuroapoptosis in a mouse model of prematurity. *J Matern Fetal Neonatal Med*:1–8.

- 633 Cao-Lormeau V-M et al. (2016) Guillain-Barré Syndrome outbreak associated with Zika virus  
634 infection in French Polynesia: a case-control study. *Lancet* 387:1531–1539.
- 635 Carod-Artal FJ (2018) Neurological complications of Zika virus infection. *Expert Rev Anti Infect*  
636 *Ther* 16:399–410.
- 637 Chimelli L, Avvad-Portari E (2018) Congenital Zika virus infection: a neuropathological review.  
638 *Childs Nerv Syst* 34:95–99.
- 639 Clancy B, Kersh B, Hyde J, Darlington RB, Anand KJS, Finlay BL (2007) Web-based method for  
640 translating neurodevelopment from laboratory species to humans. *Neuroinformatics* 5:79–  
641 94.
- 642 Costa V V et al. (2017) N-Methyl-d-Aspartate (NMDA) Receptor Blockade Prevents Neuronal  
643 Death Induced by Zika Virus Infection. *MBio* 8.
- 644 Creeley C, Dikranian K, Dissen G, Martin L, Olney J, Brambrink A (2013) Propofol-induced  
645 apoptosis of neurones and oligodendrocytes in fetal and neonatal rhesus macaque brain.  
646 *Br J Anaesth* 110 Suppl:i29-38.
- 647 Davidson AJ et al. (2016) Neurodevelopmental outcome at 2 years of age after general  
648 anaesthesia and awake-regional anaesthesia in infancy (GAS): an international  
649 multicentre, randomised controlled trial. *Lancet (London, England)* 387:239–250.
- 650 de Graaf-Peters VB, Hadders-Algra M (2006) Ontogeny of the human central nervous system:  
651 what is happening when? *Early Hum Dev* 82:257–266.
- 652 de Oliveira WK, Carmo EH, Henriques CM, Coelho G, Vazquez E, Cortez-Escalante J, Molina  
653 J, Aldighieri S, Espinal MA, Dye C (2017a) Zika Virus Infection and Associated Neurologic  
654 Disorders in Brazil. *N Engl J Med* 376:1591–1593.
- 655 de Oliveira WK, de França GVA, Carmo EH, Duncan BB, de Souza Kuchenbecker R, Schmidt

- 656 MI (2017b) Infection-related microcephaly after the 2015 and 2016 Zika virus outbreaks in  
657 Brazil: a surveillance-based analysis. *Lancet* (London, England) 390:861–870.
- 658 de Paula Freitas B, de Oliveira Dias JR, Prazeres J, Sacramento GA, Ko AI, Maia M, Belfort R  
659 (2016) Ocular Findings in Infants With Microcephaly Associated With Presumed Zika Virus  
660 Congenital Infection in Salvador, Brazil. *JAMA Ophthalmol* 134:529–535.
- 661 DeOlmos JS, Ingram WR (1971) An improved cupric-silver method for impregnation of axonal  
662 and terminal degeneration. *Brain Res* 33:523–529.
- 663 Duggal NK, Ritter JM, McDonald EM, Romo H, Guirakhoo F, Davis BS, Chang G-JJ, Brault AC  
664 (2017) Differential Neurovirulence of African and Asian Genotype Zika Virus Isolates in  
665 Outbred Immunocompetent Mice. *Am J Trop Med Hyg* 97:1410–1417.
- 666 Everett H, McFadden G (1999) Apoptosis: an innate immune response to virus infection. *Trends*  
667 *Microbiol* 7:160–165.
- 668 Fornito A, Zalesky A, Breakspear M (2015) The connectomics of brain disorders. *Nat Rev*  
669 *Neurosci* 16:159–172.
- 670 Frieden T, Bonds M, Pope A, Lurie N, Ehlinger E, McCabe E, McKay B, Joseph A, Edwards E,  
671 Stobbe M, Boyle M (2016) Transcript for CDC Telebriefing: Zika Summit Press Conference  
672 | CDC Online Newsroom | CDC. *Transcr CDC Telebriefing* April 1, 2016.
- 673 Gaburro J, Bhatti A, Sundaramoorthy V, Dearnley M, Green D, Nahavandi S, Paradkar PN,  
674 Duchemin J-B (2018) Zika virus-induced hyper excitation precedes death of mouse primary  
675 neuron. *Virol J* 15:79.
- 676 Goel MK, Khanna P, Kishore J (2010) Understanding survival analysis: Kaplan-Meier estimate.  
677 *Int J Ayurveda Res* 1:274–278.
- 678 Honein MA et al. (2017) Birth Defects Among Fetuses and Infants of US Women With Evidence

- 679 of Possible Zika Virus Infection During Pregnancy. *JAMA* 317:59–68.
- 680 Ishimaru MJJ, Ikonomidou C, Tenkova TII, Der TCC, Dikranian K, Sesma MAA, Olney JWW  
681 (1999) Distinguishing excitotoxic from apoptotic neurodegeneration in the developing rat  
682 brain. *J Comp Neurol* 408:461–476.
- 683 Jaenisch T, Rosenberger KD, Brito C, Brady O, Brasil P, Marques ET (2017) Risk of  
684 microcephaly after Zika virus infection in Brazil, 2015 to 2016. *Bull World Health Organ*  
685 95:191–198.
- 686 Kidokoro H, de Vries LS, Ogawa C, Ito Y, Ohno A, Groenendaal F, Saitoh S, Okumura A, Ito Y,  
687 Natsume J (2017) Predominant area of brain lesions in neonates with herpes simplex  
688 encephalitis. *J Perinatol* 37:1210–1214.
- 689 Lazear HM, Govero J, Smith AM, Platt DJ, Fernandez E, Miner JJ, Diamond MS (2016) A  
690 Mouse Model of Zika Virus Pathogenesis. *Cell Host Microbe* 19:720–730.
- 691 Lein ES et al. (2007) Genome-wide atlas of gene expression in the adult mouse brain. *Nature*  
692 445:168–176.
- 693 Lewis ML, Culbertson WW, Post JD, Miller D, Kokame GT, Dix RD (1989) Herpes simplex virus  
694 type 1. A cause of the acute retinal necrosis syndrome. *Ophthalmology* 96:875–878.
- 695 Lindquist MA, Mejia A (2016) Zen and the art of multiple comparisons. *Psychosom Med* 77:114–  
696 125.
- 697 McDonald JW, Johnston M V (1990) Physiological and pathophysiological roles of excitatory  
698 amino acids during central nervous system development. *Brain Res Brain Res Rev* 15:41–  
699 70.
- 700 Melo AS de O et al. (2016) Congenital Zika Virus Infection: Beyond Neonatal Microcephaly.  
701 *JAMA Neurol* 73:1407–1416.

- 702 Meneses J do A, Ishigami AC, de Mello LM, de Albuquerque LL, de Brito CAA, Cordeiro MT,  
 703 Pena LJ (2017) Lessons Learned at the Epicenter of Brazil's Congenital Zika Epidemic:  
 704 Evidence From 87 Confirmed Cases. *Clin Infect Dis* 64:1302–1308.
- 705 Miner JJ, Cao B, Govero J, Smith AM, Fernandez E, Cabrera OH, Garber C, Noll M, Klein RS,  
 706 Noguchi KK, Mysorekar IU, Diamond MS (2016a) Zika Virus Infection during Pregnancy in  
 707 Mice Causes Placental Damage and Fetal Demise. *Cell* 165:1081–1091.
- 708 Miner JJ, Sene A, Richner JM, Smith AM, Santeford A, Ban N, Weger-Lucarelli J, Manzella F,  
 709 Rückert C, Govero J, Noguchi KK, Ebel GD, Diamond MS, Apte RS (2016b) Zika Virus  
 710 Infection in Mice Causes Panuveitis with Shedding of Virus in Tears. *Cell Rep* 16:3208–  
 711 3218.
- 712 Nem de Oliveira Souza I, Frost PS, França J V, Nascimento-Viana JB, Neris RLS, Freitas L,  
 713 Pinheiro DJLL, Nogueira CO, Neves G, Chimelli L, De Felice FG, Cavaleiro ÉA, Ferreira  
 714 ST, Assunção-Miranda I, Figueiredo CP, Da Poian AT, Clarke JR (2018) Acute and chronic  
 715 neurological consequences of early-life Zika virus infection in mice. *Sci Transl Med* 10.
- 716 Ng W, Soto-Acosta R, Bradrick S, Garcia-Blanco M, Ooi E (2017) The 5' and 3' Untranslated  
 717 Regions of the Flaviviral Genome. *Viruses* 9:137.
- 718 Noguchi KK (2001) NMDA antagonist induced neurotoxicity and psychosis: the dissociative  
 719 stimulation hypothesis. In: *Handbook of Neurotoxicology: Volume II* (Massaro E, ed), pp  
 720 1582–1592. Totowa, USA: Humana Press.
- 721 Noguchi KK, Nemmers B, Farber NB (2005) Age has a similar influence on the susceptibility to  
 722 NMDA antagonist-induced neurodegeneration in most brain regions. *Brain Res Dev Brain*  
 723 *Res* 158:82–91.
- 724 Noguchi KK, Walls KC, Wozniak DF, Olney JW, Roth KA, Farber NB (2008) Acute neonatal  
 725 glucocorticoid exposure produces selective and rapid cerebellar neural progenitor cell

- 726 apoptotic death. *Cell Death Differ* 15:1582–1592.
- 727 Olmo IG, Carvalho TG, Costa V V, Alves-Silva J, Ferrari CZ, Izidoro-Toledo TC, da Silva JF,  
 728 Teixeira AL, Souza DG, Marques JT, Teixeira MM, Vieira LB, Ribeiro FM (2017) Zika Virus  
 729 Promotes Neuronal Cell Death in a Non-Cell Autonomous Manner by Triggering the  
 730 Release of Neurotoxic Factors. *Front Immunol* 8:1016.
- 731 Rasmussen SA, Jamieson DJ, Honein MA, Petersen LR (2016) Zika Virus and Birth Defects--  
 732 Reviewing the Evidence for Causality. *N Engl J Med* 374:1981–1987.
- 733 Rice ME et al. (2018) Vital Signs: Zika-Associated Birth Defects and Neurodevelopmental  
 734 Abnormalities Possibly Associated with Congenital Zika Virus Infection - U.S. Territories  
 735 and Freely Associated States, 2018. *MMWR Morb Mortal Wkly Rep* 67:858–867.
- 736 Rich JT, Neely JG, Paniello RC, Voelker CCJ, Nussenbaum B, Wang EW (2010) A practical  
 737 guide to understanding Kaplan-Meier curves. *Otolaryngol Head Neck Surg* 143:331–336.
- 738 Saad T, PennaeCosta AA, de Góes FV, de Freitas M, de Almeida JV, de Santa Ignêz LJ,  
 739 Amancio AP, Alvim RJ, Antunes Kramberger LA (2018) Neurological manifestations of  
 740 congenital Zika virus infection. *Childs Nerv Syst* 34:73–78.
- 741 Sengul G, Watson C (2015) Ascending and Descending Pathways in the Spinal Cord. In: *The*  
 742 *Rat Nervous System*, pp 115–130. Elsevier.
- 743 Torvik A (1956) Transneuronal changes in the inferior olive and pontine nuclei in kittens. *J*  
 744 *Neuropathol Exp Neurol* 15:119–145.
- 745 Tripathi S, Balasubramaniam VRMT, Brown JA, Mena I, Grant A, Bardina S V, Maringer K,  
 746 Schwarz MC, Maestre AM, Sourisseau M, Albrecht RA, Krammer F, Evans MJ, Fernandez-  
 747 Sesma A, Lim JK, García-Sastre A (2017) A novel Zika virus mouse model reveals strain  
 748 specific differences in virus pathogenesis and host inflammatory immune responses. *PLoS*  
 749 *Pathog* 13:e1006258.

- 750 Trumpy JH (1971) Transneuronal degeneration in the pontine nuclei of the cat. I. Neuronal
- 751 changes in animals of varying ages. II. The glial proliferation. *Ergeb Anat*
- 752 *Entwicklungsgesch* 44:3–72.
- 753 Tsetsarkin KA, Kenney H, Chen R, Liu G, Manukyan H, Whitehead SS, Laassri M, Chumakov
- 754 K, Pletnev AG (2016) A Full-Length Infectious cDNA Clone of Zika Virus from the 2015
- 755 Epidemic in Brazil as a Genetic Platform for Studies of Virus-Host Interactions and Vaccine
- 756 Development. *MBio* 7.
- 757 van den Pol AN, Mao G, Yang Y, Ornaghi S, Davis JN (2017) Zika Virus Targeting in the
- 758 Developing Brain. *J Neurosci* 37:2161–2175.
- 759 van der Linden H, Carvalho MD, van der Linden V, Lacerda KM, Pessoa A, Carneiro ML,
- 760 Cordeiro MT, Valente KD (2018) Epilepsy Profile in Infants with Congenital Zika Virus
- 761 Infection. *N Engl J Med* 379:891–892.
- 762 van der Linden V, Filho ELR, Lins OG, van der Linden A, Aragão M de FVV, Brainer-Lima AM,
- 763 Cruz DDCS, Rocha MAW, Sobral da Silva PF, Carvalho MDCG, do Amaral FJ, Gomes JA,
- 764 Ribeiro de Medeiros IC, Ventura C V, Ramos RC (2016a) Congenital Zika syndrome with
- 765 arthrogryposis: retrospective case series study. *BMJ* 354:i3899.
- 766 van der Linden V, Pessoa A, Dobyns W, Barkovich AJ, Júnior H van der L, Filho ELR, Ribeiro
- 767 EM, Leal M de C, Coimbra PP de A, Aragão M de FVV, Verçosa I, Ventura C, Ramos RC,
- 768 Cruz DDCS, Cordeiro MT, Mota VMR, Dott M, Hillard C, Moore CA (2016b) Description of
- 769 13 Infants Born During October 2015-January 2016 With Congenital Zika Virus Infection
- 770 Without Microcephaly at Birth - Brazil. *MMWR Morb Mortal Wkly Rep* 65:1343–1348.
- 771 Ventura LO, Ventura C V, Dias N de C, Vilar IG, Gois AL, Arantes TE, Fernandes LC, Chiang
- 772 MF, Miller MT, Lawrence L (2018) Visual impairment evaluation in 119 children with
- 773 congenital Zika syndrome. *J AAPOS Off Publ Am Assoc Pediatr Ophthalmol Strabismus*



774 22:218-222.e1.

775 Ventura C V, Maia M, Ventura B V, Linden V Van Der, Araújo EB, Ramos RC, Rocha MAW,  
776 Carvalho MDCG, Belfort R, Ventura LO (2016) Ophthalmological findings in infants with  
777 microcephaly and presumable intra-uterus Zika virus infection. *Arq Bras Oftalmol* 79:1–3.  
778 Workman AD, Charvet CJ, Clancy B, Darlington RB, Finlay BL (2013) Modeling transformations  
779 of neurodevelopmental sequences across mammalian species. *J Neurosci* 33:7368–7383.  
780 Yuan L et al. (2017) A single mutation in the prM protein of Zika virus contributes to fetal  
781 microcephaly. *Science* 358:933–936.

782

783

784 **FIGURE AND TABLE LEGENDS**

785 **Fig. 1. Quantitative analysis reveals Paraiba/2015 infection results in prolonged**  
786 **lethality/degeneration and more severe hypoplasia. [A]** Kaplan-Meier curves reveal  
787 **FP/2013** infection produces acute lethality occurring primarily between 10-17 DPI but  
788 **Paraiba/2015** infection results in almost equal lethality with deaths occurring during an  
789 expanded period between 8-24 DPI. **[B-H]** AC3 immunolabeled sections rated on our  
790 degeneration scale reveal no effect at 7 DPI, both viruses increasing apoptosis at 13 DPI, and  
791 only **Paraiba/2015** increasing apoptosis at 30 DPI. **[I-O]** Silver stained sections rated with the  
792 same scale shows infection with **FP/2013** increases degeneration between 7-13 DPI that as  
793 absent by 30 DPI. Alternatively, **Paraiba/2015** infection results in delayed argyrophilia  
794 beginning at 13 DPI that leads to prolonged degeneration extending to at least 30 DPI in several  
795 regions. **[P]** At 30 DPI, brains weights were significantly lighter for **Paraiba/2015** only. **[P-S]**  
796 Nissl stained sections had regions outlined revealing significant reductions in area for the dorsal  
797 cortex, hippocampus, and cerebellum following **Paraiba/2015** infection only. Group key and  
798 Bonferroni post-hocs values located in lower-right box. For ANOVAs and F-values see Table 1.

799

800 **Fig. 2. Histology reveals extensive degeneration that mirrors infection in the early stage**  
801 **(7-13 DPI). Frontal Cortex [A-F]: [A-B]** Silver staining reveals ZIKV exposure produces heavy  
802 degeneration 10 DPI in the frontal cortex, somatosensory (SS), caudate putamen (C/P), and  
803 septum (SE) but **[C-D]** absent in mock (MOCK) infected controls. **[E-F]** In situ hybridization  
804 (ISH) for ZIKV RNA (red) reveals infection mirrors degeneration in which pyramidal shaped cells  
805 can be distinguished (yellow arrows). **Hippocampus [G-L]: [G-H]** Infection produces  
806 degeneration in visual cortex (VIS), lateral geniculate nucleus (LGN) of the thalamus, superior  
807 colliculus (SC), and hippocampal formation including CA1, CA3, and dentate gyrus (DG).  
808 Degenerating microglia can also be seen in the dentate polymorph layer (PL), stratum oriens  
809 (SO), and stratum radiatum (SR) but is absent in controls **[I-J]** which have regions diagrammed.  
810 **[K-L]** ISH labeling reveals infection mirrors degeneration including heavy infection in granule  
811 cells (blue arrows) and pyramidal cells in CA3/CA1 (yellow arrows) but less distinct staining in  
812 the PL, SO, and SR. **Cerebellum [M-R]: [M-N]** ZIKV inoculation produces heavy argyrophilia in  
813 the granule cell layer (GCL), Purkinje cell layer (PCL; red arrows), and their connections in the  
814 molecular layer (ML) but little toxicity in the white matter (WM). **[O-P]** Mock infected controls  
815 exhibit no signs of toxicity which has regions diagrammed. **[Q-R]** ZIKV RNA was also detected  
816 in the cerebellar granule cell, Purkinje, and molecular layers mirroring toxicity in which large  
817 infected Purkinje cells (yellow arrows) could be seen. **Spinal Cord [S-V]: [S]** Degeneration was  
818 lighter in the grey matter but particularly heavy in the funiculus (white matter) including the  
819 corticospinal tract (red arrows). **[T]** No similar toxicity was seen in mock infected controls. **[U]**  
820 Activated caspase-3 (AC3) staining reveals intense apoptosis in the corticospinal tract (red  
821 arrows) along with lower levels in white and grey matter. **[V]** ZIKV infection is especially heavy  
822 in the funiculus with lower levels in the spinal grey. Outlined regions in A, C, E, G, I, K, M, O, &  
823 Q are magnified in B, D, F, H, J, L, N, P, & R respectively. Scale bars: [A-R] = 500 uM; [S-V] =  
824 100 uM.

825 **Fig. 3. Magnified views of silver staining and ISH labeling in the dentate gyrus, optic**  
826 **tract, and spinal cord.** [A-C] Argyrophilic fibers of the optic tract (arrows) could be seen  
827 degenerating in infected animals 7 DPI [A] but not in mock infected controls [B]. [C] ISH  
828 labeling for ZIKV RNA revealed punctate labeling of the optic tract (red arrows) resembling  
829 argyrophilia. [D-E] At 10 DPI, [D] degeneration can be seen in the dentate gyrus granule cell  
830 layer (GCL), molecular layer (ML) neuropil, and microglia in the polymorph layer (PL). [E] Mock  
831 infected controls exhibit no degeneration. Diagram of synaptic connections is overlaid showing  
832 axons of the perforant path synapsing with dendrites of granule cells which, in turn, send  
833 efferents through mossy fibers (MF) to CA3. [F] ISH labeling for ZIKV RNA reveals a pattern of  
834 infection that mirrors degeneration. [G] The spinal cord exhibited early infection 7 DPI that  
835 exhibited punctate labeling in the cytoplasm surrounding the nucleus in the spinal lateral horn.  
836 Scale bars = 100  $\mu$ M.

837

838 **Fig. 4. A comparison of activated caspase-3 and silver staining reveals both apoptotic**  
839 **and non-apoptotic degeneration is occurring.** Silver and activated caspase-3 (AC3) staining  
840 was performed in the same animal and region for comparison. While there was a strong  
841 correlation between the two, silver staining revealed more extensive pathology. [A] AC3  
842 labeling in the cortex shows apoptotic pyramidal cells (arrows) extending their apical dendrites  
843 to more superficial layers along with debris from less distinct cells 9 DPI. [B] Silver staining in  
844 the same region shows more extensive degeneration although it is difficult to distinguish cellular  
845 profiles. [C] Apoptosis was seen in the pyramidal and granule cells in the hippocampus along  
846 with axons of the internal capsule (a part of the corticospinal tract) projecting ventrally to the  
847 spinal cord (arrows). [D] Silver staining revealed neuronal along with heavy microglial  
848 degeneration in the hippocampus. Some fibers from the corticospinal tract can be seen in  
849 addition to degeneration in the LGN below the hippocampus. [E] AC3 immunolabeling shows  
850 numerous apoptotic granule cells in the cerebellum but far more are present with silver staining  
851 [F] along with large Purkinje cells (arrows) and argyrophilic neuropil in the molecular layer. [G-  
852 H] The corticospinal tract exhibited heavy and more distinct AC3 labeling compared to silver  
853 staining [I-J], however, more argyrophilic profiles were seen in other areas. Outlined regions in  
854 G and I are magnified in H and J respectively. Scale bar: A, B, C, D = 500  $\mu$ M; G, I = 250  $\mu$ M;  
855 E, F = 100  $\mu$ M.

856

857

858

859 **Fig. 5. ZIKV infection produces excitotoxicity, apoptosis, and other signs of pathology.**  
860 Plastic sections [A-F]: At 13 DPI, brains from ZIKV [A-C] or mock [D-F] infected animals were  
861 plastic embedded and stained with Azure II/Methylene blue. [A] ZIKV infection produced heavy  
862 vacuolization (formation of fluid filled cavities within the cytoplasm) of dentate gyrus granule  
863 cells (yellow arrows) along with abnormal nuclear chromatin condensation (red arrows). [B]  
864 Vacuolization (yellow arrows) could also be seen in the CA1 along with both dendritic swelling in  
865 the stratum oriens (red arrows) and apoptosis (black arrows). [C] Similar vacuolization (yellow  
866 arrows) and apoptosis (black arrows) was seen in the dorsal cortex (retrosplenial pictured).  
867 Control animals displayed no pathology in the dentate gyrus [D], CA1 [E], or retrosplenial cortex  
868 [F]. Electron Microscopy [G-N]: [G] Image of a normal cortical neuron exhibiting homogeneous  
869 nuclear chromatin (\*), a single nucleolus (yellow arrow), and thin endoplasmic reticulum (ER)  
870 (red arrow) within the cytoplasm. [H] Image taken 13 DPI shows cortical neuron displaying  
871 cytoplasmic condensation and vacuolated segments of ER (yellow arrow). Nuclear margination  
872 (end clumping) of nuclear chromatin (white arrows) is seen in a "clock-face profile" along with  
873 the nuclear envelope expanding into a large vacuolar space (\*). [I] Cortical neuron in a late  
874 stage of degeneration exhibiting terminal nuclear degeneration and large cytoplasmic vacuoles  
875 (\*). [J] A healthy granule cell (red arrow) among four undergoing excitotoxicity (yellow arrows)  
876 in the dentate gyrus of the hippocampus. Degenerating neurons exhibit vacuolar swelling of ER  
877 (\*) and terminal nuclear degeneration. [K] CA1 pyramidal hippocampal neuron exhibiting signs  
878 of excitotoxicity including nuclear chromatin margination forming a clock-face profile and  
879 swelling of ER undergoing vacuolization (red arrow). [L] Parenchymal hemorrhage could be  
880 seen in multiple areas of the brain with numerous red blood cells (R) lacking a nucleus  
881 interspersed among myelinated axons (yellow arrows). [M] A single lymphocyte (L) can be seen  
882 next to a heavily vacuolated (V) degenerating neuron (N). [N] A degenerating microglia (M) in  
883 the hippocampus presenting with a very condensed and shrunken cytoplasm, thin vacuolated  
884 processes, and nuclear dystrophy. Scale Bars: [A-F] = 10  $\mu$ M; [G-N] = 2  $\mu$ M.

885 **Fig. 6. Iba1 immunolabeling reveals microglia undergo initial activation followed by**  
886 **fragmentation.** [A-B] Microglia in the visual cortex (left) and hippocampus (right) after mock  
887 infection exhibit ramified microglia with thin elongated extensions with small soma indicative of  
888 an inactivated macrophage. [C-D] At 7 DPI, microglia become activated with thickened  
889 retracted processes and distended cell bodies. [E-F] By 10 DPI, microglia become less dense  
890 and begin to fragment in regions with high amounts of degeneration. Scale Bars = 100  $\mu$ M.

891

892

893 **Fig. 7. Pathology produced by French Polynesian ZIKV infection can transitions to**  
894 **pervasive apoptosis after around 13 DPI.** A small number of animals infected with **FP/2013**  
895 had degeneration transition to pervasive apoptosis. Frontal Cortex [A-D]: **[A-B]** Silver staining in  
896 the anterior cerebrum around 14 DPI shows degeneration in the caudate/putamen with intense  
897 pathology restricted to a thinning dorsal cortex. **[C-D]** AC3 immunolabeling in the same animal  
898 reveals an identical pattern of extensive apoptosis. Anterior Hippocampus [E-H]: **[E]** Silver  
899 staining reveals heavy degeneration in the cortex with slight hippocampal atrophy and  
900 ventriculomegaly (\*). **[F]** Closer examination reveals degeneration is particularly heavy in the  
901 CA3 region of hippocampus. **[G-H]** AC3 labeling mirrors silver staining indicating these cells die  
902 primarily through apoptosis. Cerebellum [I-L]: **[I-J]** Silver staining reveals heavy regions of  
903 degeneration isolated to the granule cell layer which is mirrored by AC3 labeling **[K-L]**. 30 DPI  
904 **[M-P]:** At 30 DPI, degeneration has ceased but gross morphological changes can be seen  
905 including ventriculomegaly (\*) **[M-O]** and hippocampal/cerebellar atrophy **[N-P]**. Outlined  
906 regions in A, C, E, G, I, K, M, and O are magnified in B, D, F, H, J, and L respectively. Scale  
907 Bars = 1 mm.  
908



909 **Fig. 8. Pathology produced by Paraiba/2015 infection is more virulent and almost**  
910 **exclusively apoptotic.** AC3 immunolabeling was performed at different DPI in the frontal  
911 cortex, anterior hippocampus (Ant. Hippo), posterior hippocampus (Post. Hippo), and  
912 cerebellum following infection with  $10^3$  FFU of the Brazilian ZIKV strain. **[A-D]** Apoptosis first  
913 appeared approximately 7-10 DPI with heavy degeneration in the dorsal cortex, hippocampus  
914 (CA1, CA3, and dentate gyrus), and cerebellar granule cell layer. **[E-H]** Around 10-13 DPI,  
915 apoptosis peaks often producing gross morphological changes including, dorsal cortex atrophy,  
916 hippocampal retraction dorsally, and thinning of cerebellar lobes. **[I-L]** At 20-30 DPI continuing  
917 degeneration produces microencephaly, ventriculomegaly, and atrophy of the dorsal cortex,  
918 hippocampus, and cerebellum. **[M-P]** An age matched control brain (P30) is pictured for  
919 comparison to images I-L. All images in each column are at the same magnification for  
920 comparison. Scale Bars = 1 mm.

921

922 **Fig. 9. ISH labeling for ZIKV and silver staining 10-16 after Paraiba/2015 inoculation**  
923 **reveal intense infection and degeneration mirroring apoptosis. Frontal Cortex [A-D]: [A]**  
924 ISH labeling for ZIKV RNA in the frontal cerebrum reveals intense infection in the dorsal  
925 somatosensory/motor cortex and caudate/putamen. [B] A close up of outlined region shows  
926 almost continuous labeling throughout suggesting infection in all cell types. [C-D] Silver staining  
927 reveals degeneration matching infection and AC3 labeling. [E-F] The hippocampus was also  
928 heavily infected throughout the dentate gyrus, CA1, and CA3 regions with silver staining [G-H]  
929 mirroring the pattern of infection. [I-J] ISH labeling in the cerebellum revealed dense infection  
930 within entire lobes but less severe in others. [K-L] Silver staining was more severe and  
931 particularly intense in the granule cell layer of the cerebellum. Scale bars = 1 mm.  
932

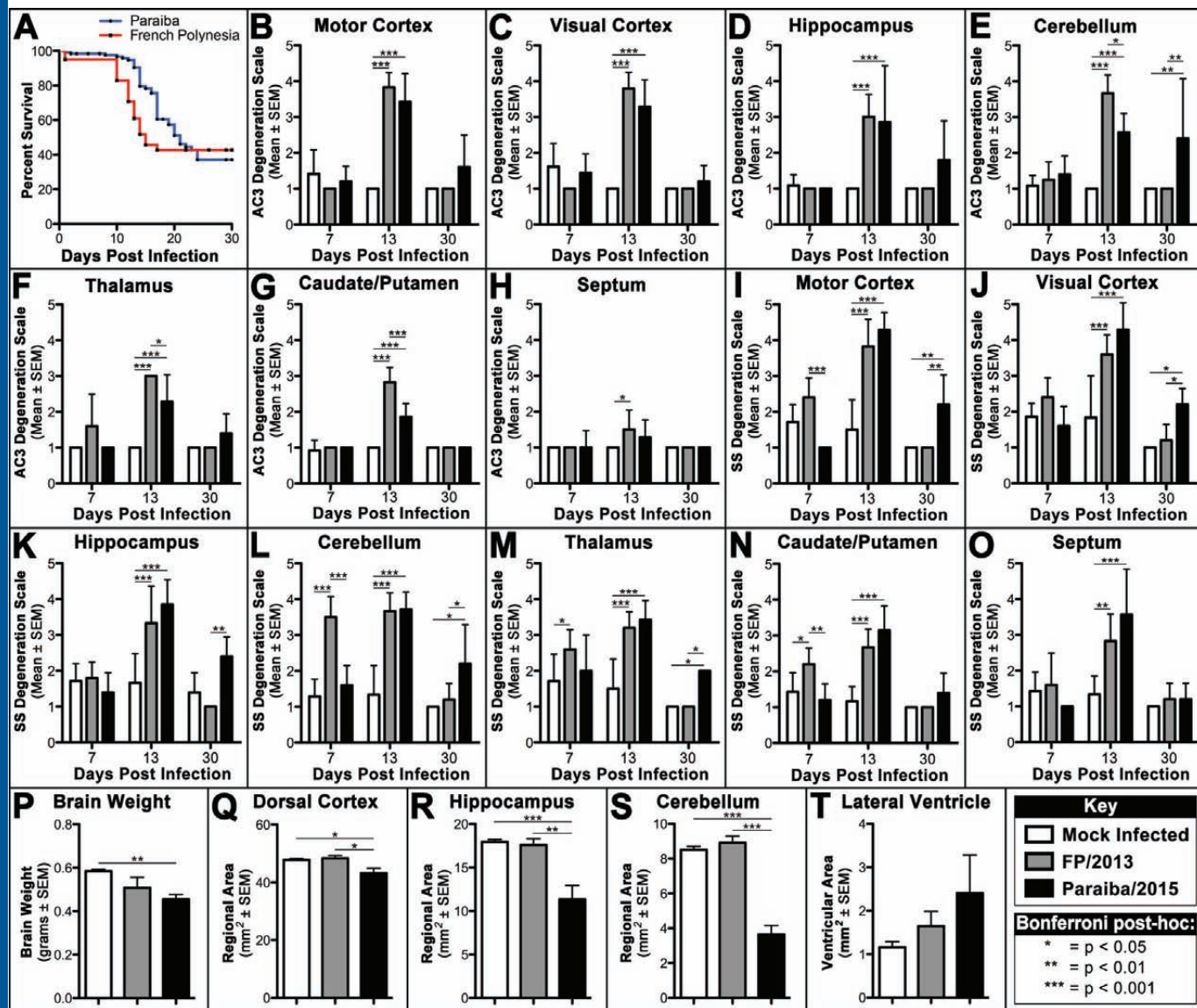
933 **Fig. 10. Labeling reveals regions with high ZIKV infection contain numerous neurons but**  
934 **more limited microglia and astrocytes at 10 days post-infection. [A-D]** Tissue was  
935 immunolabeled with the neuronal nuclear marker NeuN [A], stained with the nuclear stain DAPI  
936 [B], and ISH labeled for ZIKV RNA. A merged image [D] revealed a large number of neurons  
937 located in infected regions. [E-G] Similar staining with the microglial marker (Iba1, DAPI, and  
938 ISH for ZIKV RNA) or [I-L] astroglial marker (GFAP, DAPI, and ISH for ZIKV RNA) revealed  
939 more limited co-labeling. Scale bar = 100 uM.  
940

941 **Fig. 11. Plastic embedding and electron microscopy following infection with Paraiba/2015**  
 942 **reveals massive apoptosis, parenchymal hemorrhage, axonal pathology, and an adaptive**  
 943 **immune response.** Plastic Sections [A-C]: Mouse pups were infected with **Paraiba/2015** at  $10^3$   
 944 FFU and sacrificed 13 DPI for plastic embedding and staining with Azure II/Methylene blue.  
 945 Histology revealed a large number of cells displaying characteristic signs of apoptosis with  
 946 shrunken soma and nuclear chromatin condensation (red arrows) in the **[A]** cortex, **[B]** dentate  
 947 gyrus, and **[C]** CA1 of the hippocampus. Electron microscopy [D-G]: **[D]** Apoptotic neuron  
 948 undergoing somal shrinkage and condensation of chromatin in the nucleus (N). **[E]** Perivascular  
 949 area with hemorrhaged red blood cell (R) located outside the vascular lumen (V) is adjacent to  
 950 an activated microglia (M). An additional apoptotic cell (A) in the late stage of apoptosis can  
 951 also be seen. Its bilaminar nuclear envelope is primarily intact except for one portion where  
 952 disruption allows the nucleoplasmic contents to spill into the surrounding dystrophic cytoplasm  
 953 (arrows). **[F]** Cross section of an axon undergoing massive swelling and organelle compaction  
 954 following the breakdown of axoplasmic transport. Part of this swollen axon still retains its myelin  
 955 sheath (arrows) while the rest is demyelinated and has expanded into the surrounding interstitial  
 956 space. **[G]** Neutrophils were frequently seen in post-capillary venules in preparation for  
 957 diapedesis or in the extravascular space following extravasation. Neutrophils were observed  
 958 adjacent to the endothelium (N1 and N2), adhered to the endothelial wall (N3), or in the  
 959 extravascular space (N4). Monocytes were also seen undergoing similar transmigration (M1  
 960 and M2) or in the extravascular space (M3 and M4). This reveals an adaptive immune  
 961 response as leukocytes migrate to sites of injury/infection. Scale Bars: [A-C] = 50  $\mu$ M; [D-G] = 2  
 962  $\mu$ M.  
 963  
 964

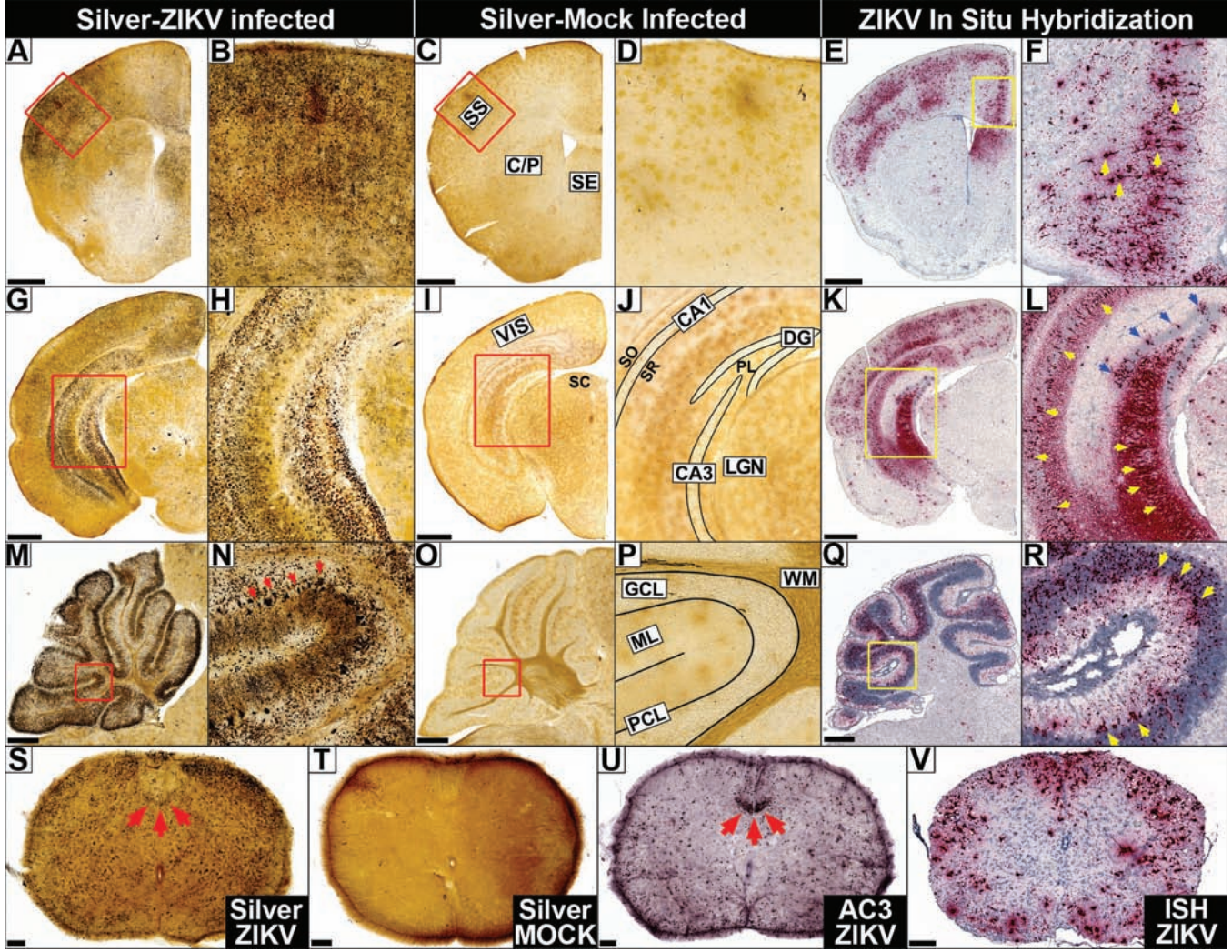
965 **Fig. 12. Infection with Paraiba/2015 produces CA3 excitotoxicity, cerebellar calcification,**  
966 **and reductions in microglia.** While AC3 labeling reveals little apoptosis in the hippocampal  
967 CA3 region [A], silver staining shows much more argyrophilia [B] suggesting non-apoptotic  
968 death is occurring. [C] Semithin plastic sections with Azure II/Methylene blue staining in CA3  
969 show the classical signs of both apoptosis (black arrows) and excitotoxicity which includes  
970 vacuolization (yellow arrows) and nuclear margination (red arrows). [D] Alizarin staining shows  
971 calcification is localized to the granule cell layer and present in atrophied lobes. [E] Iba1  
972 labeling shows microglia are present at a much lower density or are almost entirely missing from  
973 a cerebellar lobe (red arrow). Note the adjacent brain stem contains a normal density of  
974 microglia. [F] Iba1 labeling in an age matched control shows a normal density and distribution  
975 of microglia. Note severe cerebellar hypoplasia in images D-E when compared to F which is at  
976 the same magnification scale. Scale bars: [A-C] = 50  $\mu$ M; [D-F] = 1 mm.

977

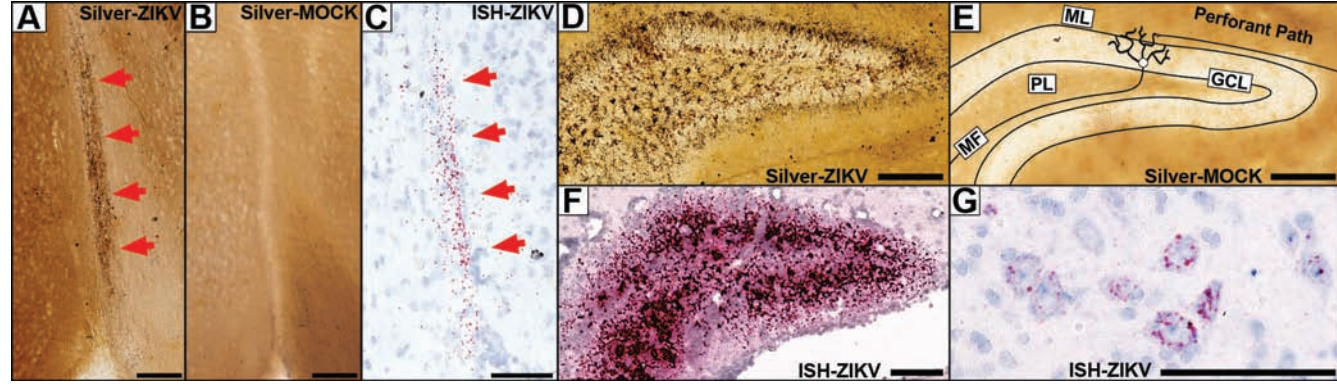
978 **Table 1. Statistical results from ANOVAs in Figure 1.** Main effects, interactions, F-values,  
979 and p-values for one- and two-ANOVAs graphed in Figure 1. \*indicates value would be non-  
980 significant following Bonferroni correction for multiple comparisons.  
981



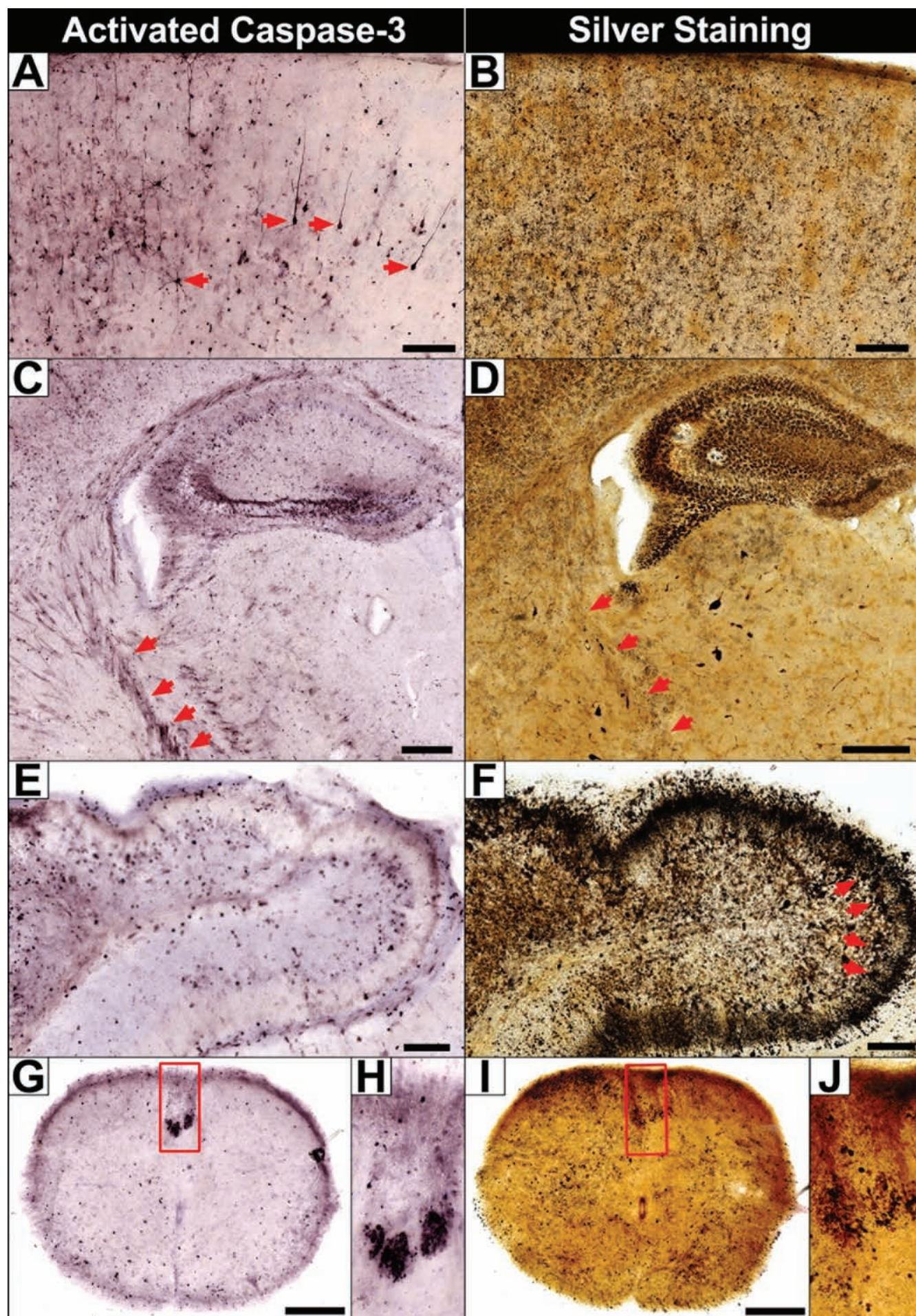




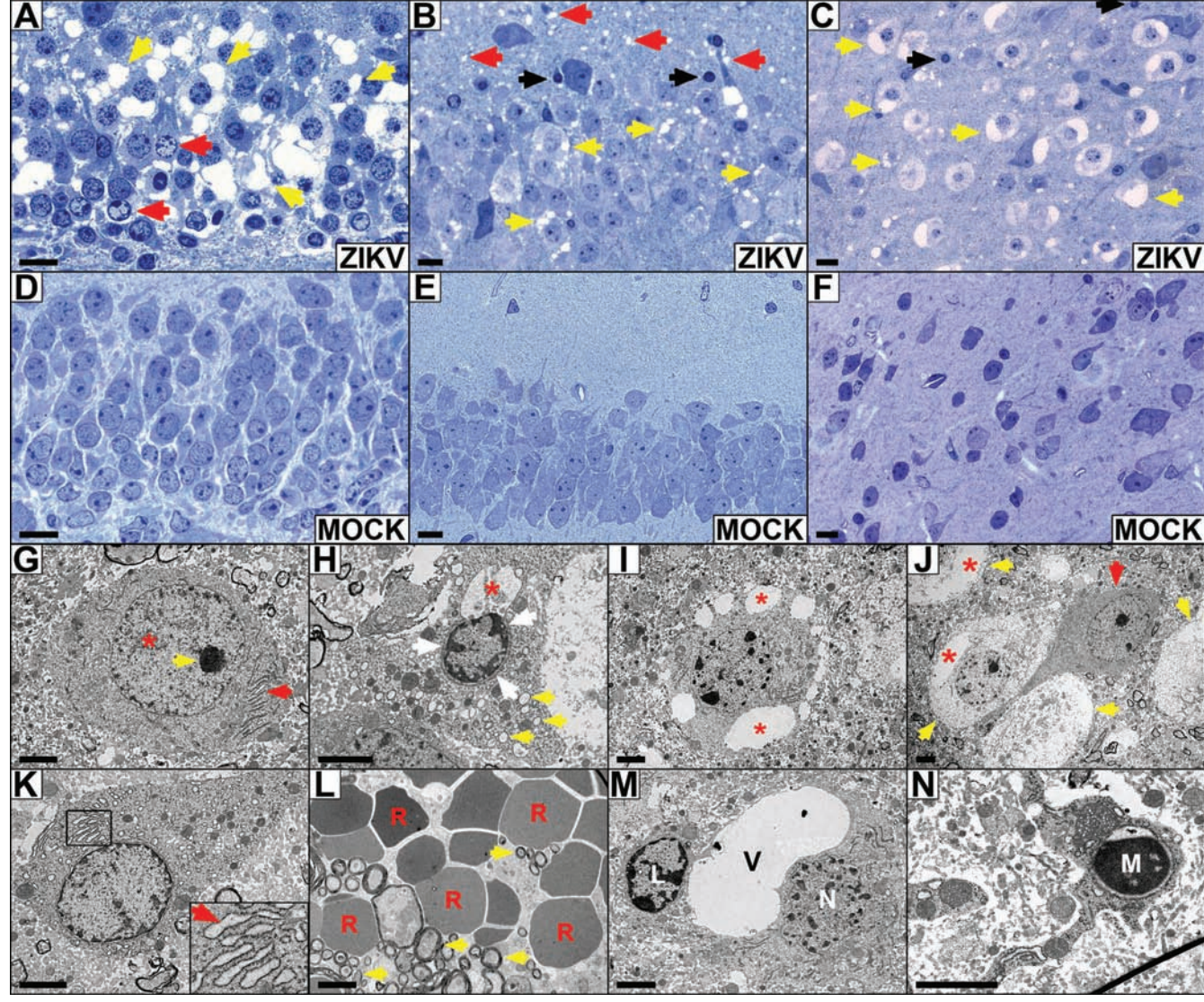




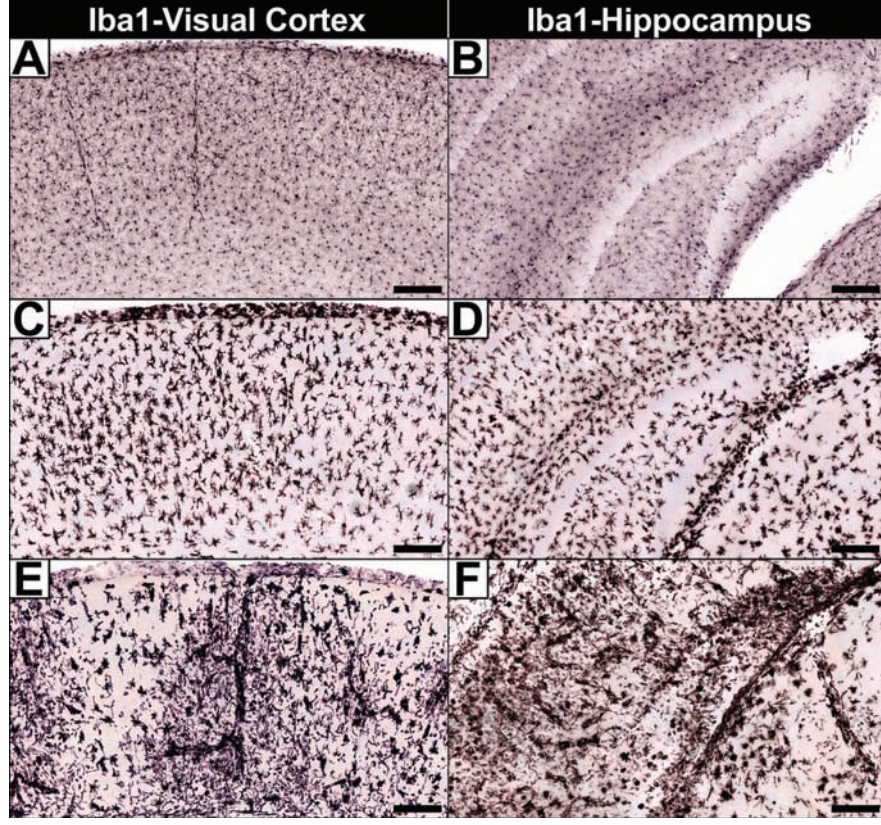




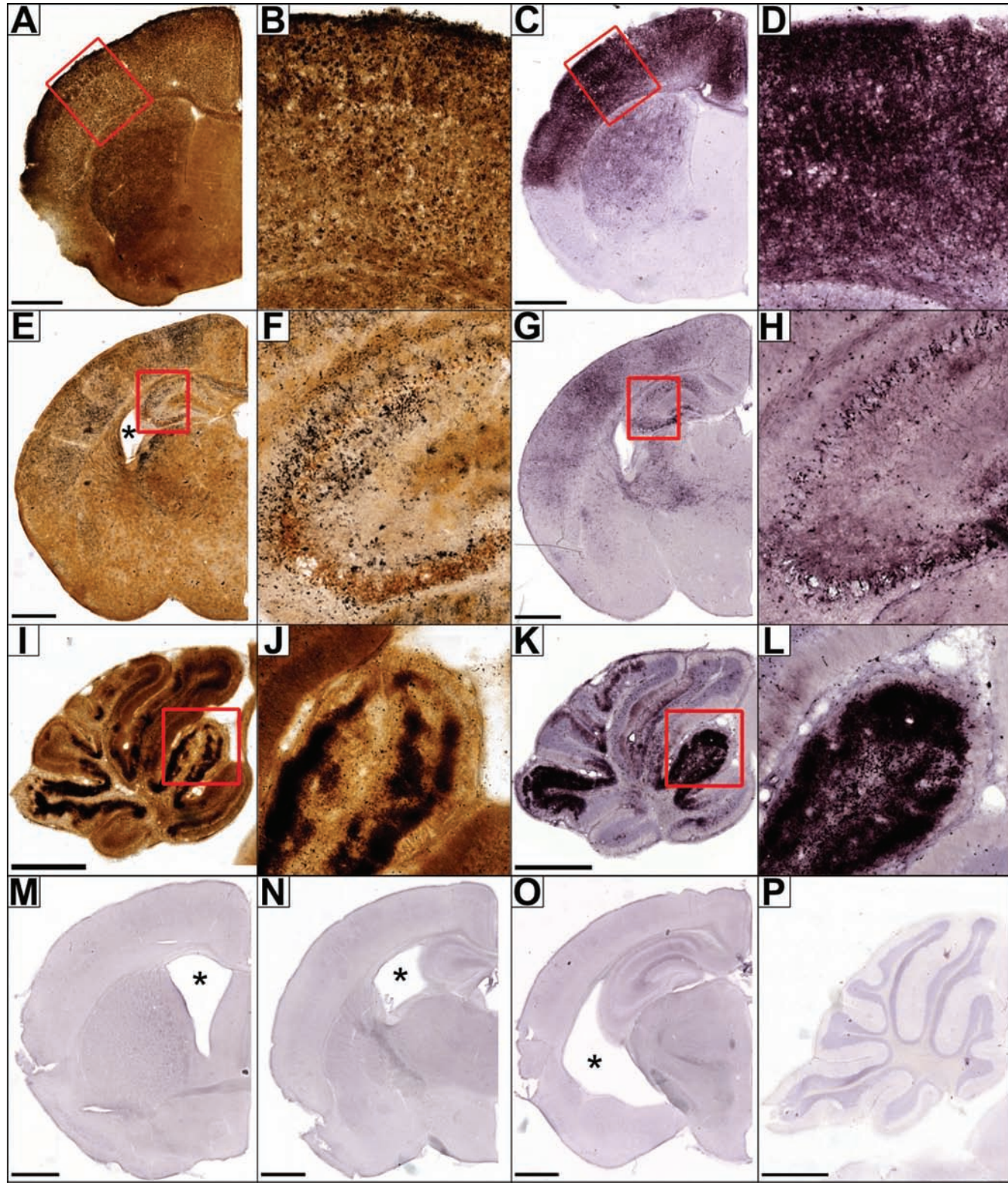




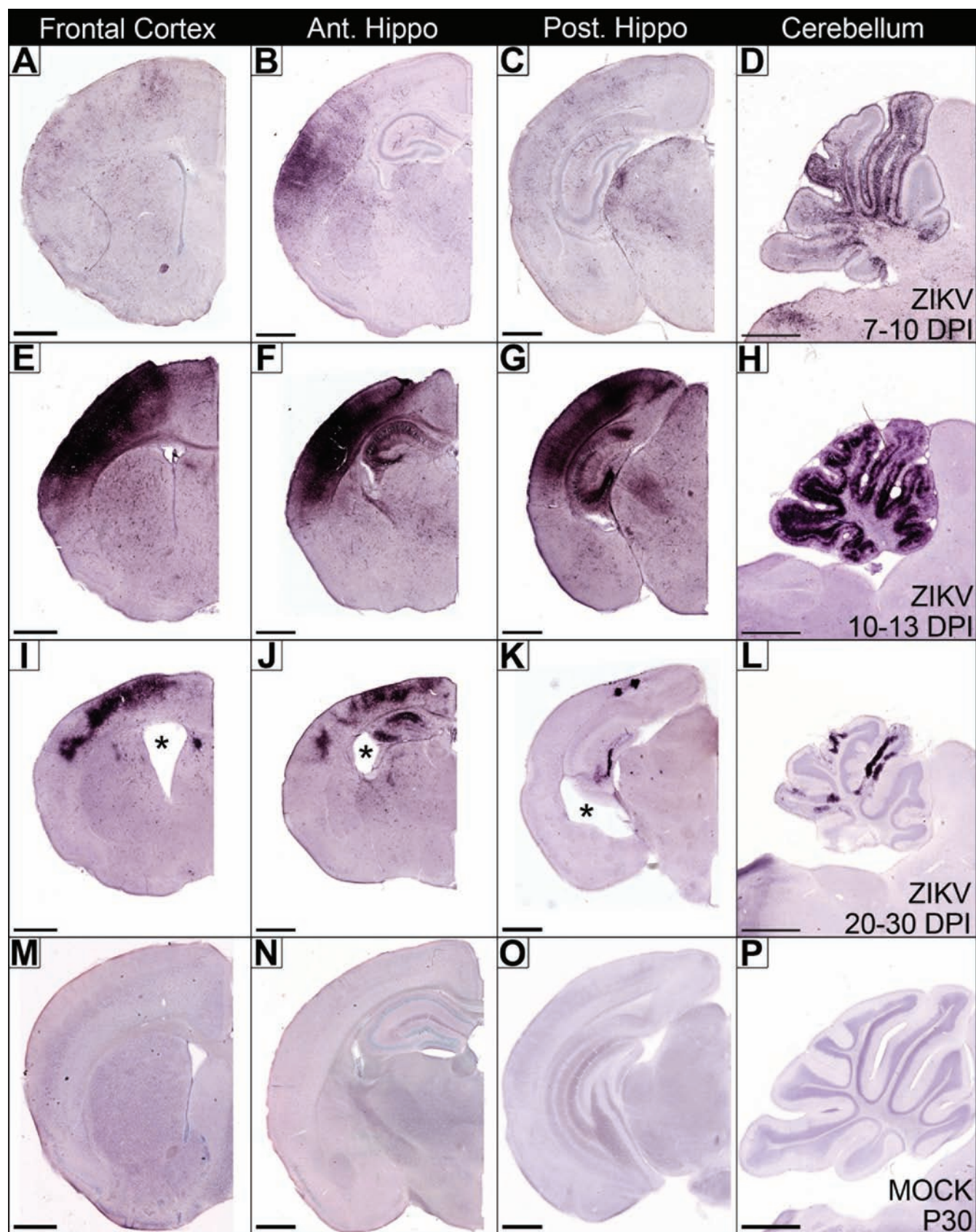




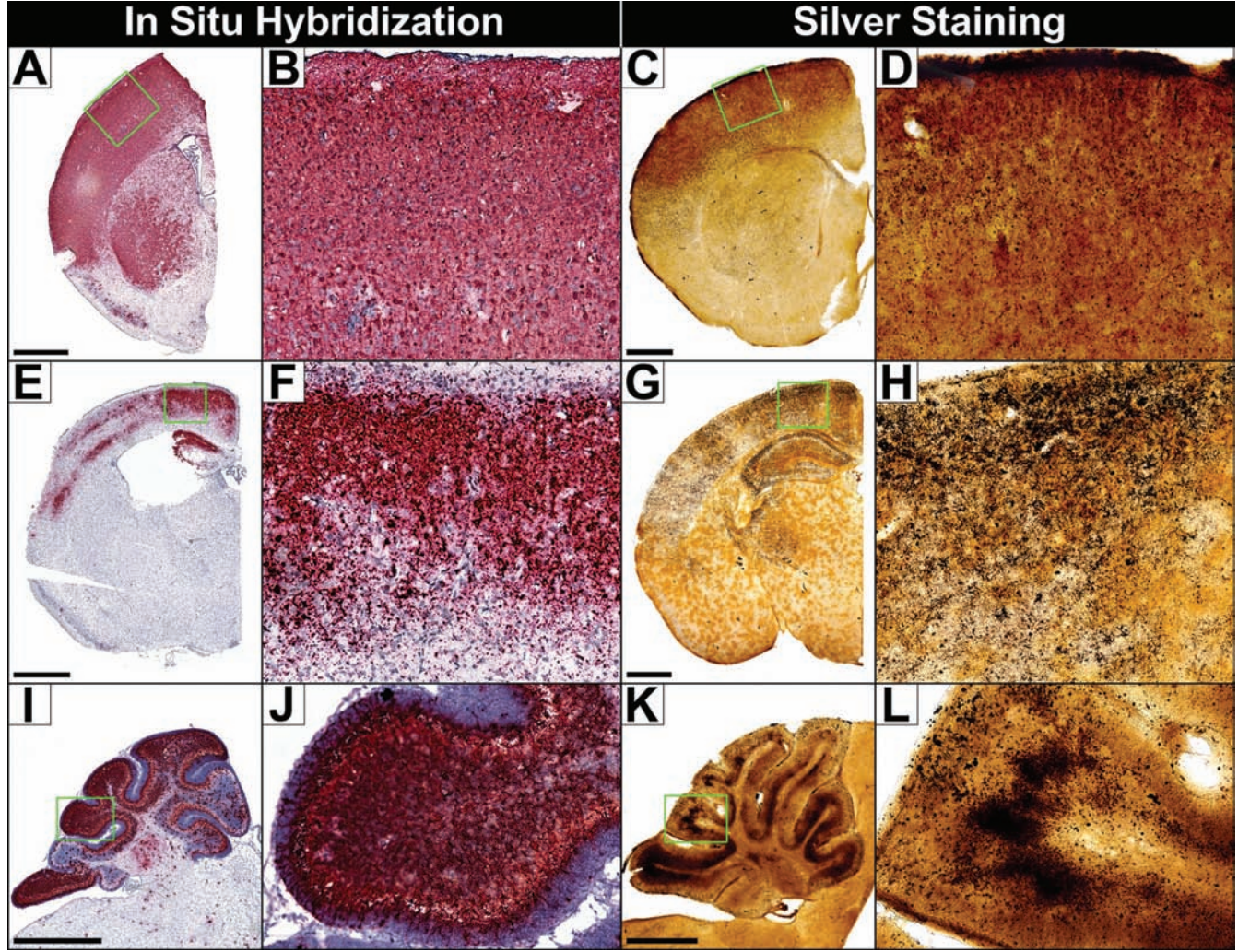


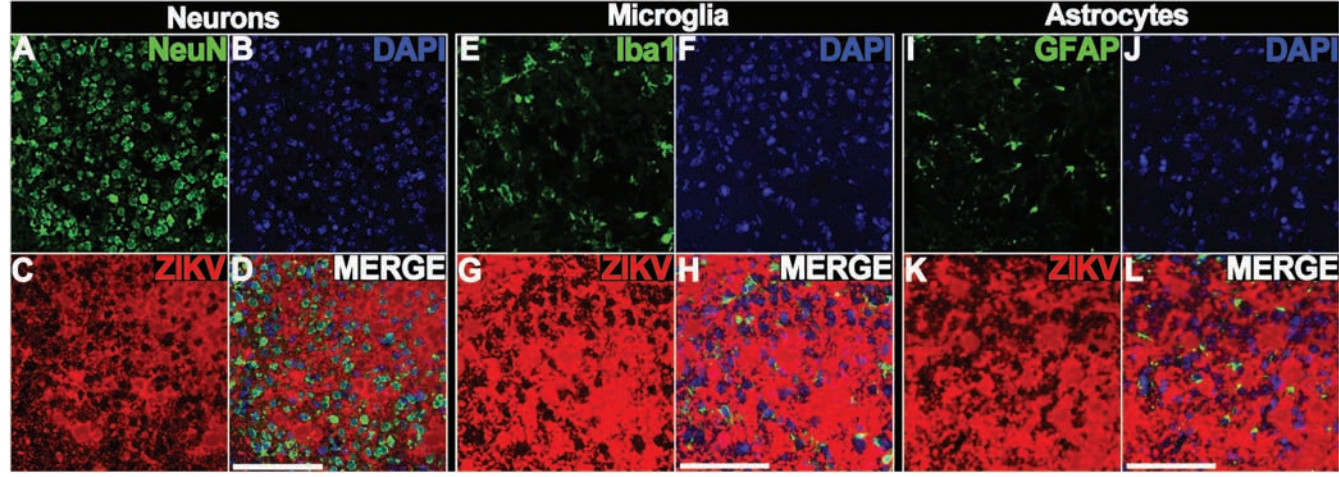




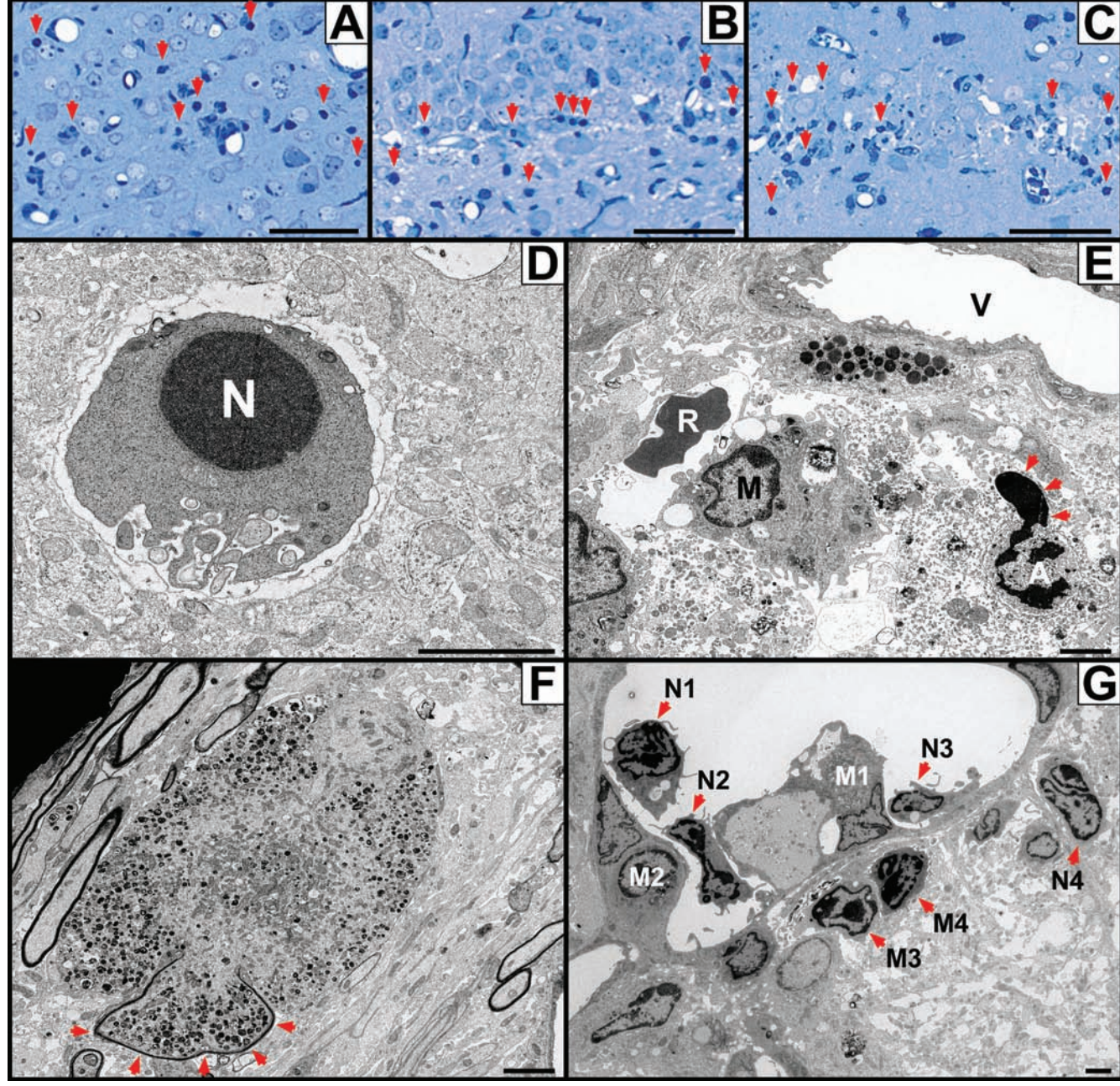


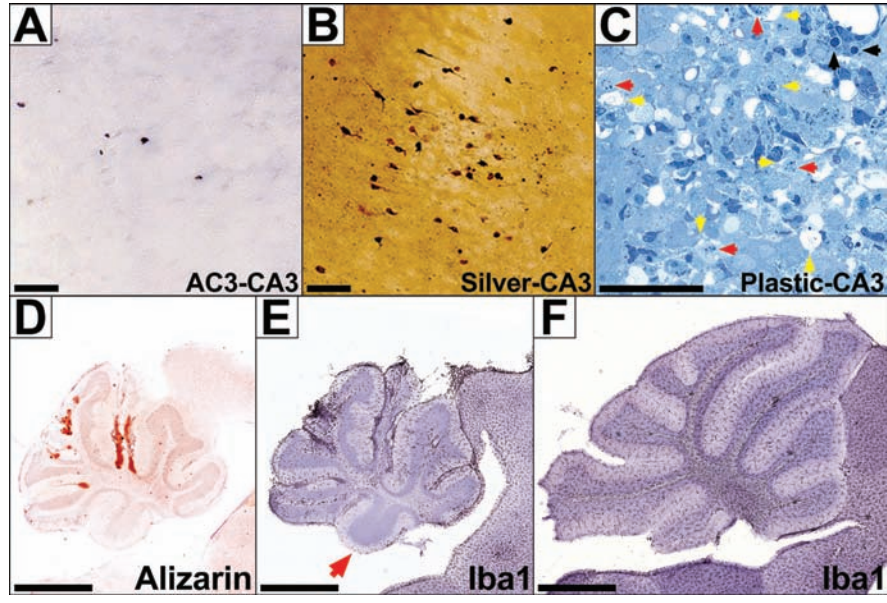














Region	Marker	Treatment	Days Post-Infection	Interaction
Hippocampus	AC3	$F[2,40] = 05.30, p = 0.0091^*$	$F[2,40] = 12.40, p < 0.0001$	$F[4,40] = 04.36, p = 0.0051$
Motor Cortex	AC3	$F[2,51] = 16.65, p < 0.0001$	$F[2,51] = 51.87, p < 0.0001$	$F[4,51] = 18.74, p < 0.0001$
Visual Cortex	AC3	$F[2,50] = 13.44, p < 0.0001$	$F[2,50] = 54.07, p < 0.0001$	$F[4,50] = 21.13, p < 0.0001$
Striatum	AC3	$F[2,51] = 36.11, p < 0.0001$	$F[2,51] = 97.88, p < 0.0001$	$F[4,51] = 31.70, p < 0.0001$
Thalamus	AC3	$F[2,40] = 15.91, p < 0.0001$	$F[2,40] = 23.75, p < 0.0001$	$F[4,40] = 08.51, p < 0.0001$
Cerebellum	AC3	$F[2,39] = 13.32, p < 0.0001$	$F[2,39] = 16.67, p < 0.0001$	$F[4,39] = 09.22, p < 0.0001$
Septum	AC3	$F[2,40] = 01.54, p = 0.2227$	$F[2,40] = 05.03, p = 0.0113^*$	$F[4,40] = 01.54, p = 0.2096$
Hippocampus	Silver Stain	$F[2,42] = 09.29, p = 0.0005$	$F[2,42] = 23.93, p < 0.0001$	$F[4,42] = 07.96, p < 0.0001$
Motor Cortex	Silver Stain	$F[2,42] = 19.55, p < 0.0001$	$F[2,42] = 49.65, p < 0.0001$	$F[4,42] = 18.59, p < 0.0001$
Visual Cortex	Silver Stain	$F[2,41] = 14.15, p < 0.0001$	$F[2,41] = 34.46, p < 0.0001$	$F[4,41] = 07.85, p < 0.0001$
Striatum	Silver Stain	$F[2,42] = 13.31, p < 0.0001$	$F[2,42] = 26.44, p < 0.0001$	$F[4,42] = 10.38, p < 0.0001$
Thalamus	Silver Stain	$F[2,41] = 14.75, p < 0.0001$	$F[2,41] = 21.77, p < 0.0001$	$F[4,41] = 05.19, p = 0.0018$
Cerebellum	Silver Stain	$F[2,41] = 30.81, p < 0.0001$	$F[2,41] = 22.43, p < 0.0001$	$F[4,41] = 11.29, p < 0.0001$
Septum	Silver Stain	$F[2,42] = 04.81, p = 0.0132^*$	$F[2,42] = 20.97, p < 0.0001$	$F[4,42] = 05.67, p = 0.0010$
Dorsal Cortex	Nissl Stain	$F[2,21] = 06.48, p = 0.0064$	N/A	N/A
Hippocampus	Nissl Stain	$F[2,19] = 15.41, p < 0.0001$	N/A	N/A
Cerebellum	Nissl Stain	$F[2,19] = 62.60, p < 0.0001$	N/A	N/A
Lateral Ventricle	Nissl Stain	$F[2,19] = 01.78, p = 0.1965$	N/A	N/A
Brain Weight	N/A	$F[2,19] = 20.58, p < 0.0001$	N/A	N/A